NASA/TM–20260003620

A Summary of Test and Analysis Results from a Second Lift+Cruise Full-Scale Drop Test

Justin D. Littell, Jacob B. Putnam, Emilie R. Baker, Nathaniel W. Gardner, Matlock M. Mennu
Langley Research Center, Hampton, Virginia

May 2026

NASA STI Program Report Series

Since its founding, NASA has been dedicated to the advancement of aeronautics and space science. The NASA scientific and technical information (STI) program plays a key part in helping NASA maintain this important role.

The NASA STI program operates under the auspices of the Agency Chief Information Officer. It collects, organizes, provides for archiving, and disseminates NASA's STI. The NASA STI program provides access to the NTRS Registered and its public interface, the NASA Technical Reports Server, thus providing one of the largest collections of aeronautical and space science STI in the world. Results are published in both non-NASA channels and by NASA in the NASA STI Report Series, which includes the following report types:

- TECHNICAL PUBLICATION. Reports of completed research or a major significant phase of research that present the results of NASA Programs and include extensive data or theoretical analysis. Includes compilations of significant scientific and technical data and information deemed to be of continuing reference value. NASA counterpart of peer-reviewed formal professional papers but has less stringent limitations on manuscript length and extent of graphic presentations.

- TECHNICAL MEMORANDUM. Scientific and technical findings that are preliminary or of specialized interest, e.g., quick release reports, working papers, and bibliographies that contain minimal annotation. Does not contain extensive analysis.

- CONTRACTOR REPORT. Scientific and technical findings by NASA-sponsored contractors and grantees.

- CONFERENCE PUBLICATION. Collected papers from scientific and technical conferences, symposia, seminars, or other meetings sponsored or co-sponsored by NASA.

- SPECIAL PUBLICATION. Scientific, technical, or historical information from NASA programs, projects, and missions, often concerned with subjects having substantial public interest.

- TECHNICAL TRANSLATION. English-language translations of foreign scientific and technical material pertinent to NASA's mission.

Specialized services also include organizing and publishing research results, distributing specialized research announcements and feeds, providing information desk and personal search support, and enabling data exchange services.

For more information about the NASA STI program, see the following:

- Access the NASA STI program home page at http://www.sti.nasa.gov

- Help desk contact information:

https://www.sti.nasa.gov/sti-contact-form/
and select the "General" help request type.

NASA/TM–20260003620

A Summary of Test and Analysis Results from a Second Lift+Cruise Full-Scale Drop Test

Justin D. Littell, Jacob B. Putnam, Emilie R. Baker, Nathaniel W. Gardner, Matlock M. Mennu
Langley Research Center, Hampton, Virginia

National Aeronautics and
Space Administration

Langley Research Center
Hampton, Virginia 23681-2199

May 2026

Available from:

NASA STI Program / Mail Stop 050
NASA Langley Research Center
Hampton, VA 23681-2199

Table of Contents

Abstract 2
Introduction 2
Test Article Development 4
  General Test overview 4
  Cabin Section Fabrication 4
  Mass Configuration 5
  Energy Absorbing Structure 8
  Instrumentation 10
  Photogrammetry 14
Test Results 16
  Airframe Accelerations 20
  Photogrammetry Results 25
  Seat Performance 32
  ATD Results 34
Model Development 42
Model Results 50
Discussion 58
Summary 61
References 62

Abstract

The realization of advanced air mobility markets is enabling new forms of transportation to take shape in the United States and around the world. Though currently in development, as these markets mature, new types of vertical take-off and landing (VTOL) vehicles have been undergoing development for use. There are many factors which must be addressed prior to these types of vehicles becoming viable alternative forms of transportation in these markets. These factors include incorporation into the existing airspaces, the logistics of operating in urban environments, along with numerous factors associated with safety and reliability.

To address some of the safety aspects associated with the development of these new types of vehicles, NASA has been conducting research into the performance of an example electric VTOL (eVTOL) aircraft as a part of the Revolutionary Vertical Lift Technology (RVLT) project. Over the course of this research, many aspects including the development of energy absorbing components, the evaluation of seating systems, the development of advanced finite element material model systems and the acquisition of full-scale vehicle impact data were investigated.

The report will discuss aspects related to the acquisition of full-scale vehicle data which occurred in the form of a full-scale impact test conducted in the Summer of 2025. This test was on a NASA designed Lift+Cruise composite cabin test article and represented a partial capstone in the entirety of previous eVTOL research conducted for the project. In this test, a variety of experiments were included in order to investigate the effect of a full-scale environment on the experiment results.

In parallel, the development of a computational impact model to simulate the full-scale test will be discussed in this report. A model of the Lift+Cruise test article was developed utilizing data collected from previous sub- and full-scale test data and then simulated in the current test environment. The model development, its use in pre-test predictions, and its use in post-test correlation will all be presented.

This report will present the test data acquired from the Lift+Cruise test and document several of the results obtained. One intended result is to determine the effect of a complex full-scale crash impact on the identification of occupant injury risk within seat and vehicle designs. A second intended result is to determine whether high-fidelity models can be used with some confidence in the prediction of test events and can allow for additional test cases to be simulated without the need of having to conduct additional tests.

The overall goal of the test is to provide the community with data that can be used for design, development or certification efforts, along with providing data on what an example eVTOL crash incident could entail.

Introduction

Advanced Air Mobility (AAM) has the potential of providing what could be the largest changes to the aviation markets since the advent of the jet engine. The market size could triple by the early 2030's [1] and with this type of growth, the number of vehicles providing services such as package delivery, medical support, firefighting, personal transportation along with many others may be commonplace.

However, in the United States (US), before this potential can be realized, there will need to be regulations in place to allow for their safe and successful operation within the US airspace. Regulations will eventually need to cover vehicle operational constraints, air traffic management, weather, security, safety and a host of others prior to operation. Various organizations, including those from academia, government and industry, are investigating many of these issues in parallel to facilitate market maturity. NASA is one of those entities investigating various aspects of AAM, researching subjects such as air traffic management [2], noise [3], ride quality [4] and a host of others. Under the Revolutionary Vertical Lift Technology (RVLT) project, a team of researchers have been investigating the safety of occupants and vehicle crashworthiness to help to fill in gaps that currently exist.

When discussing various aspects of crashworthiness for eVTOL vehicles, there are several factors that need to be considered. There are a handful of companies that have built and flown prototype eVTOL vehicles and are getting closer to being certified for flight operations in the United States. Through the development process, there have been accidents reported [5] [6], and these provided some insight into how these vehicle behave during a crash event. However, since there has not been widespread adaptation of eVTOL vehicles (of any type) into airspaces, large data sets regarding their performance during a crash event are not available. To partially address this gap, NASA has undertaken steps to develop a reference eVTOL vehicle design, which possesses similar attributes to many of the vehicle designs currently under development, and test it in what is hoped to be a relevant operational environment.

NASA has developed several reference vehicles for study [7], and while some of the initial crashworthy studies conducted by RVLT researchers examined the quadcopter [8], the reference vehicle that was developed for the full-scale test program was the Lift+Cruise (L+C) design. This design was chosen due to similarities with some of the current commercial flying prototypes. The L+C vehicle features a cabin section capable of holding 6-8 occupants, an overhead wing with multiple tiltable rotors, and a lightweight composite material system. This vehicle design was turned from a paper-only concept vehicle to a developed prototype though a test and analysis campaign [9]. After the development and fabrication of the L+C test article, it was used for evaluation of a variety of experiments in full-scale testing.

The first L+C test (L+C #1) was conducted at NASA Langley Research Center (LaRC) in November of 2022. This test featured six onboard Anthropomorphic Test Devices (ATDs, a.k.a. crash test dummies), several energy absorbing seats, and a large amount of overhead mass, which represented the wingbox structure, rotors, motors and batteries used for flight. The test parameters were primarily developed through the use of computational modelling with test data to support the model design. The results from this test have been published [10], however are summarized here for completeness. The accelerations at the belly level were over 100 g but attenuated to approximately 40 to 50 g at the floor level, in part due to the crushable subfloors. The ATDs experienced loading levels that were over the Federal Aviation Administration (FAA) certification limit of 1,500 lb. [11] in the rigid seats, but loading levels were attenuated to below the limit in the energy absorbing (EA) seat.

One major result from this test was the collapse of the cabin structure, leading to intrusion of the overhead mass into the cabin section, which potentially affected passengers in the rear rows of seats. This event was not observed in pre-test model predictions. Post-test component level testing from components removed from the test article provided evidence that several failure parameters used in the material definitions overestimated the actual failure in the actual test article. These parameters were adjusted based on the post-test component level testing, which provided improved post-test correlation results between the test and the model [12].

After L+C #1, researchers focused efforts on the further development of seat parameters, along with the redesign of the subfloor crushable structure. Details in this process can be found in ref [13]. During this process, the decision was made to fabricate a second L+C test article to use as a capstone for the technology developed in the follow-up effort. The second L+C test (L+C #2) utilized lessons learned from the first test and included several additional and different experiments. The developed L+C #2 computational model utilized improvements in the materials from subsequent component level testing, along with lessons learned from L+C #1. The L+C #2 test and model results will be the focus of this report.

Test Article Development

General Test overview

The test was conducted at the Landing and Impact Research Facility (LandIR), located at NASA LaRC. This facility is a 240-ft tall, 400-ft long, steel structure capable of lifting and swinging full-scale aircraft for crash testing under a variety of impact orientations, velocities and surfaces. A picture of the LandIR facility is shown in Figure 1.

Figure 1. LandIR facility

The test conditions selected were similar to L+C #1. Velocities of 42 ft/s in the horizontal and 26 ft/s in the vertical were chosen to represent “severe but survivable” conditions, based on accident data along with previous testing conducted at NASA LaRC [14]. However, this test included a component of yaw in the impact orientation of the test article in order to produce a three-dimensional loading condition in the test article during impact. A yaw of 10 degrees was chosen since the component level seat tests required for FAA certification in rotorcraft include this factor in the tests [11]. The impact surface was concrete. Several months were necessary to build up from an empty cabin section to a fully outfitted and instrumented test article.

Cabin Section Fabrication

The cabin section was originally made via a mold and vacuum bagging process. Molds were fabricated for the port and starboard sides of the cabin section such that each side could be made separately. The molds included cutouts for the frames so the frames and all other stiffening structures were created in-situ with each side. The skin and frame components consisted of 6 layers and 8 layers, respectively, of a 3k-70 Plain Weave carbon fiber oriented in a repeating $[+45°/ -45°]_N$ pattern, infused with INF-114 resin, placed into the mold and set in a vacuum while the resin cured. After each side mold was completed, they were combined and post-cure bonded. A picture of the mold and port side structure post-mold is shown next in Figure 2.

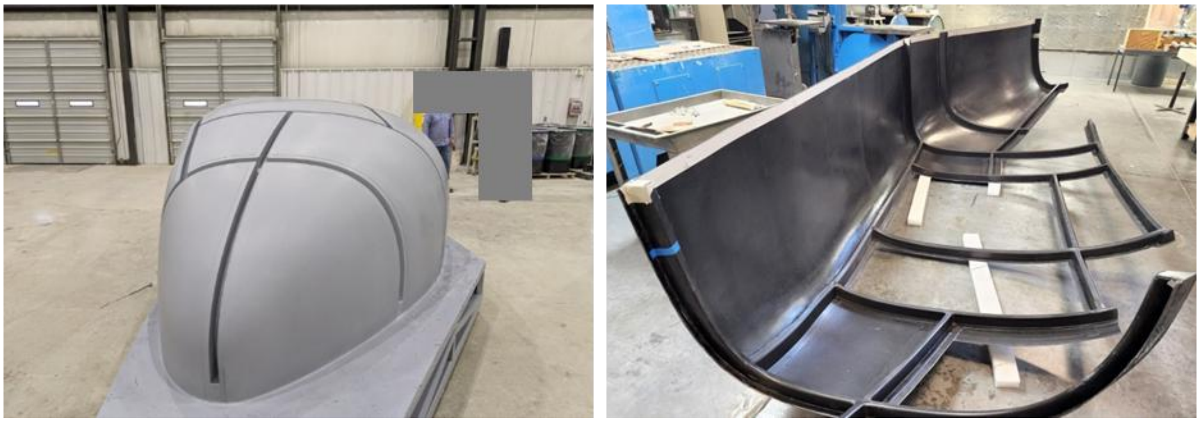

Figure 2. L+C mold (left) and port side vehicle structure (right)

There were several notable changes from the L+C #1 cabin section. The first was the removal of the rear panel behind the rear seats. This panel was originally intended to be a rear bulkhead, but it did not offer any additional structural properties to the cabin. The second was the windscreen material. The windscreen used for L+C #2 was a Fluid Glass 1" deep pour epoxy kit.

The process for creating the windscreen started by utilizing the composite molds. The epoxy was partially cured as a flat surface. Halfway through the curing process, while the material had stiffness but was formable, the epoxy was pressed into the composite molds using a heat gun. After removal from the molds, it was fastened to the cabin section composite structure utilizing rivets and composite hinges.

Mass Configuration

Mass was added to the cabin section through the addition of ballast. A ballast mass of 576 lb. was added to the tail in the form of large steel plates to account for the tail structure. This mass is shown in Figure 3.

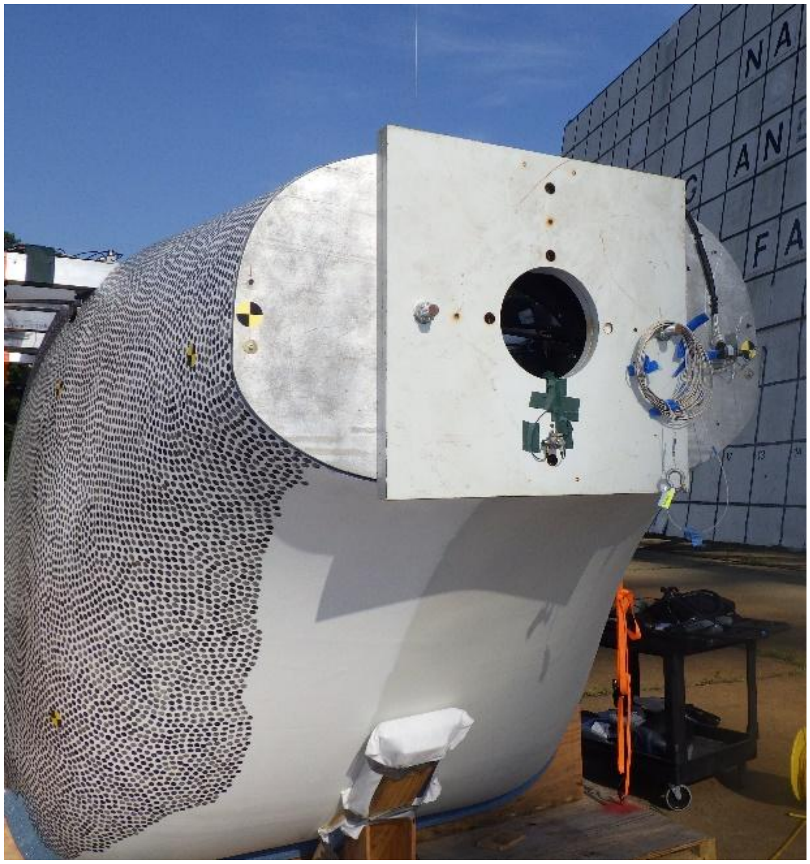

Figure 3. Tail ballast mass

Similar to L+C #1, the test article utilized ballast for the overhead mass. The ballast was represented by lifting hardware, which, in addition to functioning as the ballast representing the overhead wing mass, rotors, motors and batteries, allowed the test article to interface with the LandIR facility through the use of cable attachment points which would be necessary for lifting and swinging the test article into the impact surface.

However, unlike the first L+C #1 test, this test condition assumed that the overhead mass would represent a breakaway or semi-frangible overhead wing design, which would subsequently offload most of the overhead mass in the impact. This failure mode has been produced in at least one documented eVTOL accident [6], and also has been shown to occur in other types of aircraft tests [15]. Thus, a lighter lifting fixture was fabricated by utilizing an aluminum structure instead of steel box beam. The lifting fixture from L+C #1 was approximately 1,080 lb., while the lifting fixture for this test was only 394 lb., representing a difference of 686 lb., or approximately a 64% mass reduction.

The assumed impact conditions for L+C #2 differed from the first test in that they included a 10-degree yaw. This change necessitated the addition of components to the lifting structure that would orient the test article at a 10-degree nose-South angle as referenced to the test flight path velocities. A picture of the lifting hardware, prior to installation is shown in Figure 4.

Figure 4. Lifting hardware

One area of research under the RVLT project included the study of the performance of Energy Storage System (ESS, a.k.a. battery) components under dynamic impacts at the ESS component level [16][17]. For this reason, an underfloor ESS installation was added to the test as a way of obtaining data to compare and contrast to data obtained at the component level. Since there are hazard issues in performing experiments on live, fully charged ESS systems, the decision was made to include the ESS experiment as a mass addition simulating a small ESS pack. A rigid fixture was developed and mounted below the rear rows of seats, which simulated the inclusion of this small pack. The top of the fixture represented the floor section and had two openings in which ballast mass could be added. Since actual ESS configurations may differ in their total mass, this configuration allowed the addition of variable amounts of mass depending on what configuration was desired. For the specific test configuration, the ESS ballast mass was 110 lb. on each side, with the floor structure weighing 92 lb., bringing a total underfloor weight to 312 lb. This addition also allowed for the examination of the effect of an underfloor ESS installation on occupants seated above. It was hypothesized that the rigidity of the ESS ballast mass and fixture would increase the loading levels experienced in the occupants. The ESS fixture and ballast mass is shown in Figure 5.

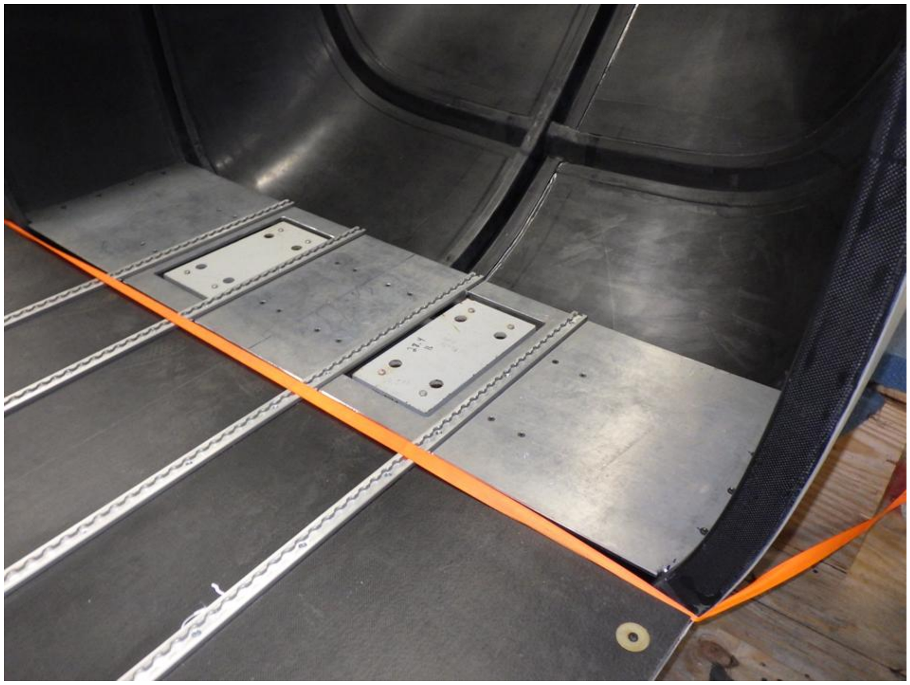

Figure 5. ESS mounting fixture and ballast mass

Energy Absorbing Structure

Energy attenuating subfloors were designed to provide light weight and modular subfloor structures which could effectively absorb vertical impact energy in a full-scale impact environment without collapsing under combined axes loading. The geometric design featuring corrugated walls and in the top-down shape of an infinity symbol was designed based on lessons learned from the triangular cruciform subfloor used in the L+C # 1 test. The EA subfloor design is shown in Figure 6. Expanding from the previous design, the corrugation curvature was extended in order to produce a more stable and uniform vertical crush and the triangular cruciform was replaced with the infinity shape in order to reduce the force required for crush initiation. The reduced crush initiation force was deemed essential to improve the combined performance of subfloor and seat EA systems. The subfloors were composed of 4 layers of a hybrid carbon-Kevlar composite material with Epon 828 resin system at a $[+45°/ -45°]_2$ orientation. The EA subfloor was approximately 7.5 in. tall. The EA subfloor was developed through a combination of finite element (FE) analysis and component level testing the full details of which can be found in [8].

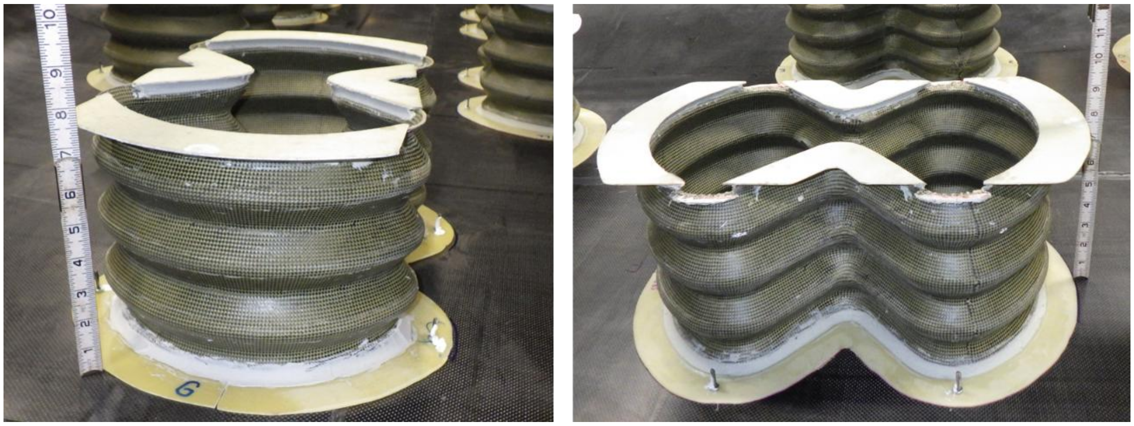

Figure 6. EA subfloor design

The EA subfloors were positioned within the airframe such that they were directly under the seat above and oriented with the long direction of the subfloor parallel to the seated occupant. Seats 1-4 were positioned on top of the EA subfloors covering the first two rows of the test article. The EA subfloors utilized flat flanges on each side which were bonded and riveted to the belly skin on one side and bonded to the bottom of the floor panel on the other. Two EA subfloors were positioned behind the second row of seats, directly underneath the onboard data acquisition system (DAS) hardware. While the DAS hardware was ruggedized and has been used for multiple tests, the additional expected attenuation from the subfloor crush would help to protect the DAS hardware and data collected. The rear rows of seats were above the rigid ESS experiment. The positioning of the EA subfloor in the airframe is shown in Figure 7.

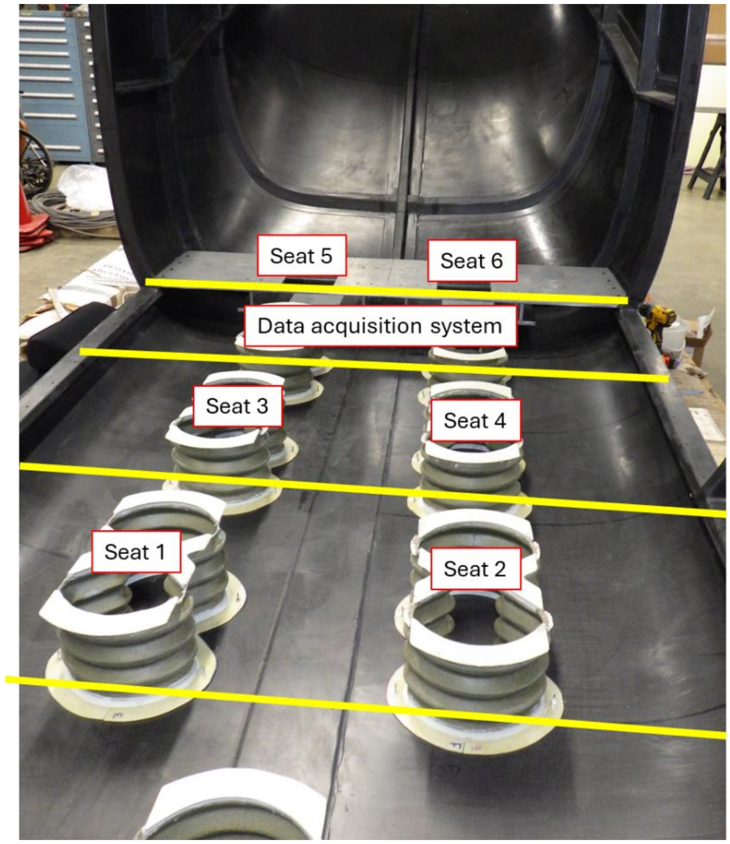

Figure 7. EA subfloor components installed in their location (floors not installed)

Instrumentation

The test article was instrumented primarily with a suite of accelerometers installed at various locations to capture response across the entirety of the airframe and occupants. Accelerometers captured three axis data; x – longitudinal, y – lateral, and z – vertical, and had full-scale ranges of 2,000 g in the vertical and 500 g in the longitudinal and lateral directions. The sensor layout is shown in Figure 8.

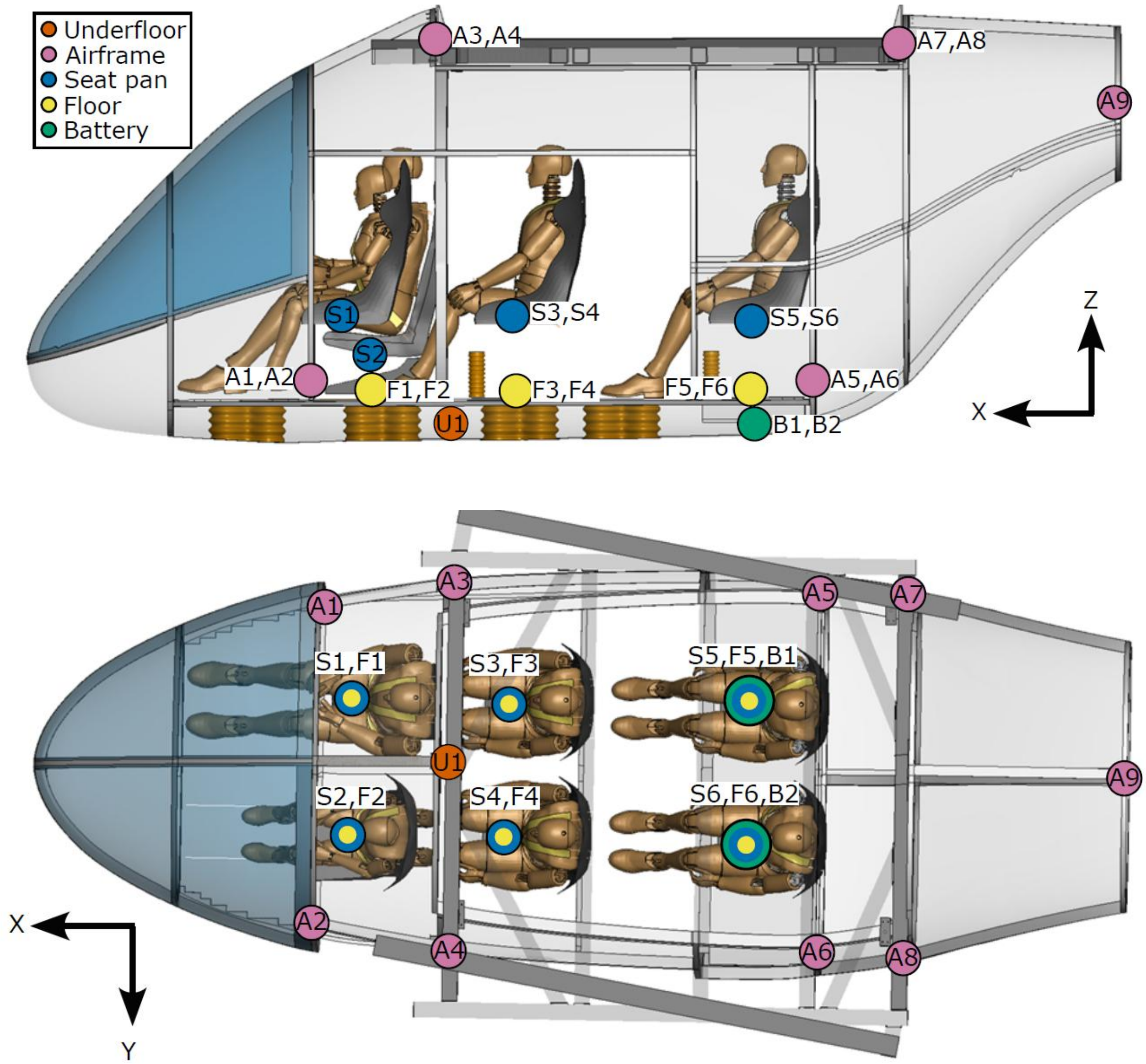

Figure 8. Instrumentation layout. Side view (top) and top view (bottom)

Locations identified in the figure are the approximate positions where the sensors were installed. A single location was identified for the underfloor or belly acceleration (U1). This location was similar to the location chosen for L+C #1. For the airframe itself, sensors were placed at the A-pillars (A1, A2), C-pillars (A5, A6), and floor locations below the seats (F1-F6). The ballast mass was instrumented in several locations. The overhead mass contained four sensor locations (A3, A4, A7, A8), which measured accelerations at the forward and aft attachment locations for both the port and starboard sides. The tail ballast was instrumented at a single center location, and the ESS ballast on both the port and starboard sides was instrumented (B1, B2).

In addition to the instrumentation of the airframe, the test article was fitted with six anthropomorphic test devices (ATDs, a.k.a. crash test dummies). The ATDs varied in size which ranged to include one Hybrid

III (H3) 95^{th} percentile male, one H3 5^{th} percentile female, two FAA H3 50^{th} percentile males, and two Hybrid II (H2) 50^{th} percentile males. Each ATD was seated in a unique seat for the purpose of conducting several seat-to-seat comparisons. Half of the seats were rigid in design, which meant they contained no energy absorbing crushable structure in the seat legs capable of attenuating the impact energy. Two of the seats included a NASA designed energy attenuation system [8], which utilized EA crush tubes developed for the L+C #1 test. One of the seats was a commercial off-the-shelf (COTS) seat which included its own attenuation system. The seats utilized either carbon fiber composite or aluminum seat buckets. These buckets were then either attached onto a rigid seat leg base, composed of aluminum frames, or a seat leg base containing the EA tubes. Seats containing the EA tubes are labeled as "NASA EA" seats in this report. Seats used either a 3- or 4-point harness for ATD restraints. An example of the types of seats used in the test is shown in Figure 9.

Figure 9. Example seat types used. Rigid (left), NASA developed EA (middle), COTS (right)

There have been considerable characterization efforts completed to develop the NASA EA seat. After the development of the initial EA tubes for the L+C #1 test, numerous follow on vertical drop tests were conducted utilizing this seat configuration in a variety of input pulse shapes, ATD and loaded condition variations on indoor drop towers located at NASA LaRC [18]. These tests were conducted to evaluate the EA system under these variables in order to gauge performance and efficiency.

There were two major updates to the design of the EA tubes that resulted from the testing, and both were incorporated to accommodate the loading of all three sized ATDs (5^{th}, 50^{th} and 95^{th}). First, the number of composite layers used within the tubes increased from four layers to five layers. Second, the usable crush distance of the tube was extended by approximately two inches, from 5.5 in. to 7.5 in. to allow for additional energy attenuation prior to tube compaction. This resulted in a new tube height of approximately 10 in. versus the original 8-in. tubes. However, since these tests were conducted under vertical loading only, there were still outstanding questions as to the efficiency of the crush performance in a combined horizontal and vertical loading condition, which can only be evaluated at the full-scale level. Even though the crush performance was unknown in combined loading conditions, the decision was made to proceed using the 5-layer, 10-inch-long EA tubes in the full-scale test, noting the deficiencies identified by the purely vertical loading condition of the drop tower testing.

For the L+C #2 test, all seat pans were instrumented with triaxial accelerometers recording three-axis measurements. Due to slight differences in the ATD builds, the ATD instrumentation was slightly different between them, but in all instances, data in the form of accelerations were collected in the head, chest and pelvis of each ATD, along with loads and moments in the lumbar spine. For the H3 ATDs which featured an articulating neck, upper neck forces and moments were collected. All onboard accelerometer and ATD data were collected via the onboard data acquisition system (DAS), which sampled at 10 kHz. A tabular layout of each seat and ATD is shown in Table 1.

Table 1. ATD Layout

Location	ATD	Seat base - bucket	Seat belt
Seat 1 – Front Starboard	H3 95th	COTS	4 pt
Seat 2 – Front Port	H3 5th	Rigid - Composite	4 pt
Seat 3 – Middle Starboard	FAA H3 50th	Rigid - Composite	4 pt
Seat 4 – Middle Port	FAA H3 50th	NASA EA - Composite	4 pt
Seat 5 – Rear Starboard	H2 50th	Rigid - Aluminum	3 pt
Seat 6 – Rear Port	H2 50th	NASA EA - Aluminum	3 pt

A suite of high-speed cameras was utilized in the test, as shown in Figure 13. Several of the cameras were positioned in the four cardinal directions to gather overall vehicle motion from all four sides. Two cameras were positioned at isometric angles with respect to the flight path to capture the vehicle motion from a forward position due to the included yaw in the impact condition. Two cameras were positioned perpendicular to the port side of the vehicle for high-speed photogrammetry, which included marker tracking and three-dimensional Digital Image Correlation (3D-DIC). All cameras shared a common, middle-trigger recording function and were synchronized with an IRIG timecode such that the camera data could be directly compared to DAS data utilizing a common timecode post-test. The camera resolution was set to between 2 and 4 megapixels (MP) depending upon the camera system used and the desired application. The higher resolution cameras were used for 3D-DIC, while the lower resolution cameras were used for viewing the entire vehicle and areas of interest during the approach, impact and subsequent slide out during the test. The cameras were set up to acquire images at 1 kHz with a continuous write-overwrite loop to the cameras buffer until the manual trigger event. Total recording duration varied between the camera systems based on the available volatile memory of each camera.

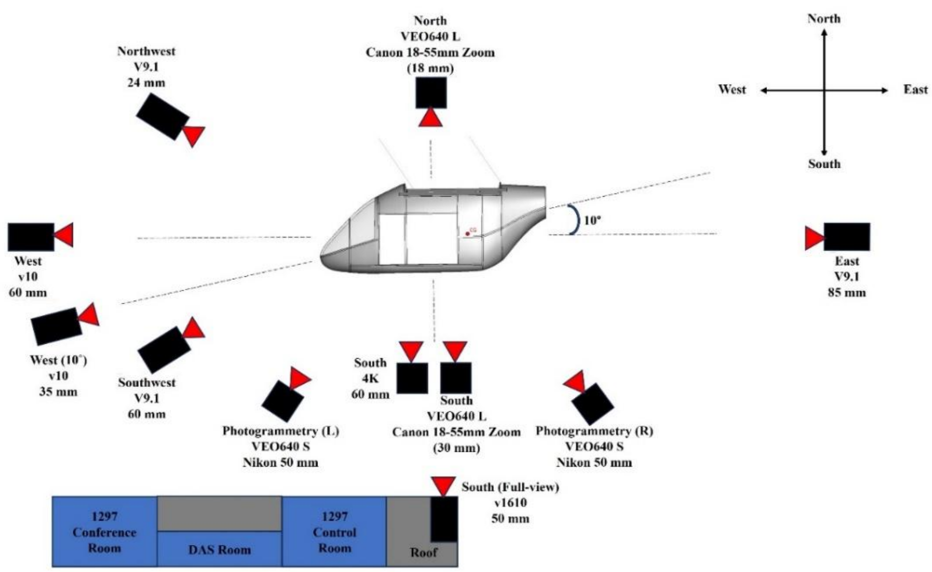

Figure 10. High-speed camera setup

Photogrammetry

High-speed photogrammetry, consisting of both 3D-DIC and marker tracking was implemented during the test. 3D-DIC was selected as the primary measurement technique to characterize the full-field displacement and strain of the port side of the test article. Marker tracking was used to track the two-dimensional position and motion of bowtie markers that were manually placed in specific areas-of-interest to acquire impact conditions and subsequent motion of the vehicle. Impact conditions included horizontal velocity, vertical velocity, pitch, roll and yaw.

Prior to testing, the port side of the vehicle was wiped clean with a cloth to minimize any surface contamination. A thin base coat of white paint was applied via a paint roller, providing a uniform high-contrast background. A random, black stochastic speckle pattern was applied to the surface using a custom-made rubber stamp with a speckle size of approximately 3/8 in. The speckle pattern on the port side of the vehicle is shown in Figure 11.

Figure 11. Speckle pattern on port-side of vehicle for 3D-DIC

Once the speckle pattern was applied, and sufficient time had passed to allow for the paint to dry, bowtie markers were positioned at specific locations for marker tracking. Bowties were positioned externally on the lifting hardware and fuselage, as well as internally on the ATD's, seats and EA tubes, as shown in Figure 12. After the bowties were positioned and affixed to the vehicle, the distances between each bowtie were carefully measured and recorded.

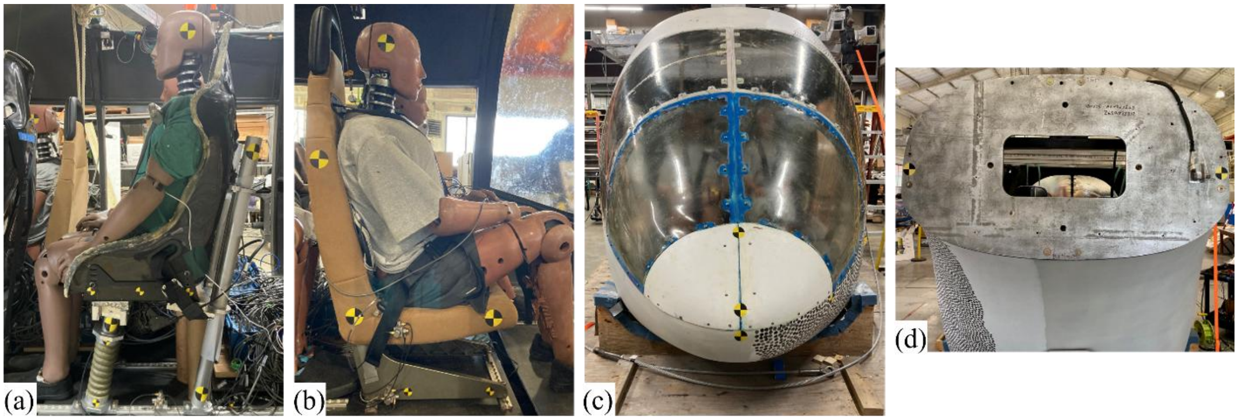

Figure 12. Bowtie marker positions (a) NASA EA Seat + H3 50th ATD, (b) COTS seat + H3 95th ATD, (c) Nose and (d) Tail

The test article was connected to the LandIR facility cables utilizing the lifting hardware on the top of the section. The cabling systems lifted the test article up to the required 35 feet of drop height and the test sequence began. A picture of the test article in its test configuration just prior to lifting is shown in Figure 13.

Figure 13. Test article prior to testing.

Test Results

The test was conducted on June 26, 2025, at the NASA LaRC LandIR facility. The test article impacted concrete at 38 ft/s horizontal velocity, 28 ft/s vertical velocity, a 0.1-degree pitch (nose down), a 2.7-degree roll (starboard side low), and a 16.7-degree yaw (port side South). Examination of the high-speed videos showed that several notable events occurred. These notable events are shown in Table 2.

Table 2. Notable event timing

Event	IRIG Time (s)	Time after impact (s)
Impact-Front	36.835	0.000
Impact-Back	36.847	0.012
Seat 6 Stroke Begin	36.857	0.022
Seat 1 Stroke Begin	36.867	0.032
Maximum Floor Crush	36.878	0.043
Seat 6 Stroke End	36.884	0.049
Seats 2 and 3 Maximum Displacement	36.893	0.058
Nose rebounds off ground	36.912	0.077
Motion Stop	39.877	3.042

The notable events demonstrate that the majority of the energy attenuation occurred in the first 0.058 seconds (s) of the test, which was similar to the results obtained from L+C #1. Unlike L+C #1, the roof did not collapse, and the test article rebounded by exhibiting a nose up pitch shortly after the time the maximum crush occurred. The duration of the test, as measured by when the motion stopped was approximately 3.042 seconds. The test image sequence from the port side is first shown in Figure 14.

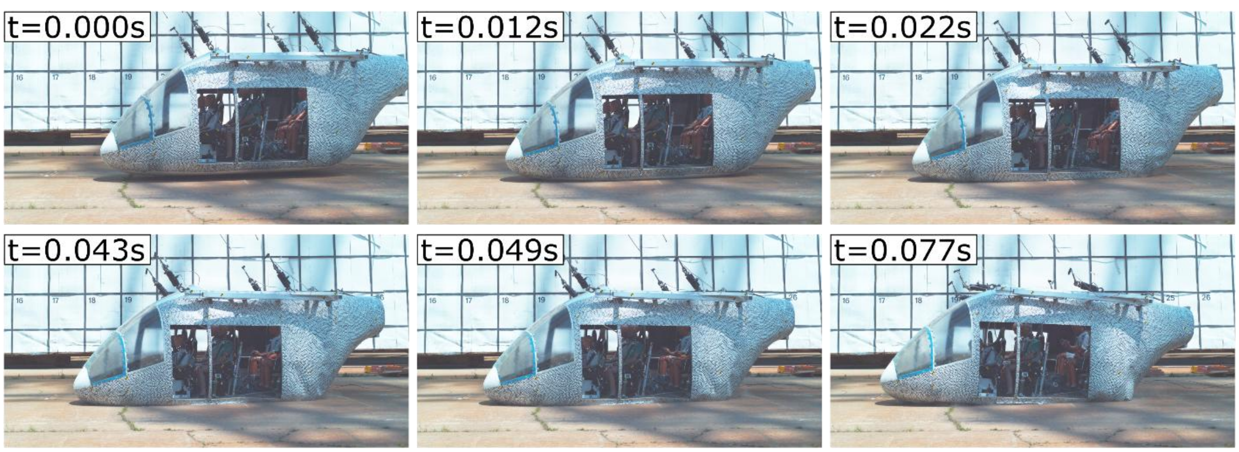

Figure 14. Port Side Image Sequence

The upper left image in Figure 14 shows the test article at impact, which occurred first on the starboard front side. Due to the geometry of the belly of the test article, the rear area near the C-pillar impacted approximately 0.012 s later, which is shown in the upper middle image. Subfloor crush began immediately after impact. The upper right image depicts the time when Seat 6, which is located on the rear port side over the rigid ESS experiment, began to stroke. Shortly after this event, the front COTS seat began to stroke (t=0.032 s after impact, not shown), and shortly thereafter at 0.043 s after impact, the subfloor reached its maximum compression, which can be seen in the lower left image, noting the lack of any white surface underneath the door due to the crushed subfloor. The lower middle image shows the time of maximum displacement in Seat 6, while the lower right image shows the beginning of the rebound. The same time sequence image series is next shown for the starboard side in Figure 15.

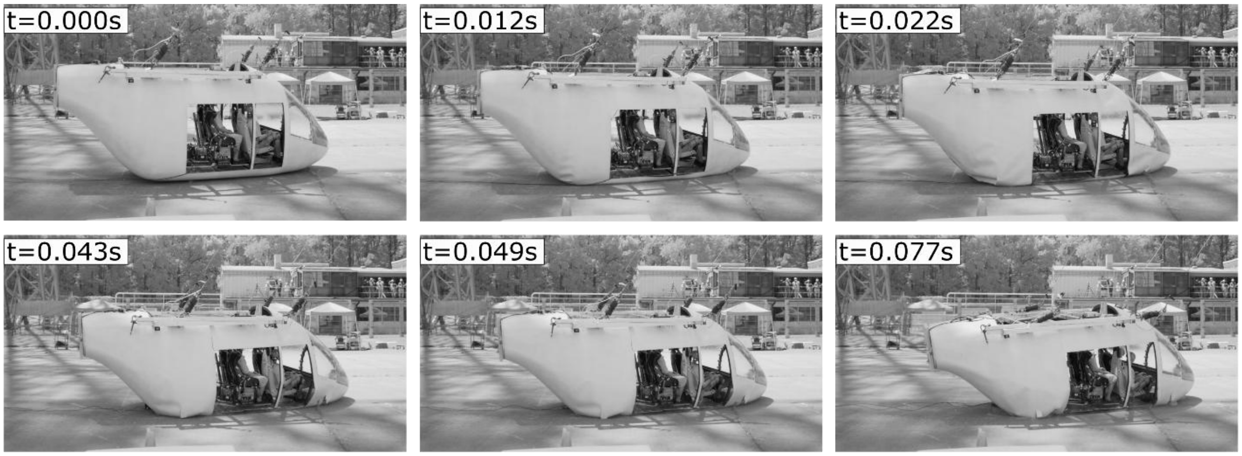

Figure 15. Starboard Side Image Sequence

It is noted that the yaw that occurred in the test is much more visible when examining the angle of the test article during the image sequence from the starboard side. Since the yaw positioned the nose South, the nose of the vehicle pointed away from the Northside camera, allowing more visibility into the forward portion of the cabin. Another noticeable result is that the majority of the airframe deformation and failures occurred on the starboard side. The A-pillar and B-pillar on the starboard side show failure at 0.030 s and 0.034 s after impact, respectively, which can be observed in the bottom left image. Other items of interest include a split that occurred on the top of the A-pillar, near the windscreen, and also multiple failures that have occurred near the rear row of seats. All of these items were inspected immediately following the test. The post-test configuration of the test article immediately following the test is shown next in Figure 16.


Figure 16. Post-test configuration of the test article. Port side (left) and Starboard side (right)

The damage to the A- and B-pillars can be seen in Figure 16, right. Even with this damage, the cabin integrity remained intact. Portions of the windscreen cracked, however, during further inspection, these cracks were due to one of the cable components used to swing the test article making contact with the windscreen and not the test or test article itself. The test article, along with the onboard ATDs, came to rest after a slide out of 45 feet, with a slight nose up pitch, nose left yaw, and starboard side roll. The starboard side pillars are next shown in Figure 17, highlighting the mid-span failure location.

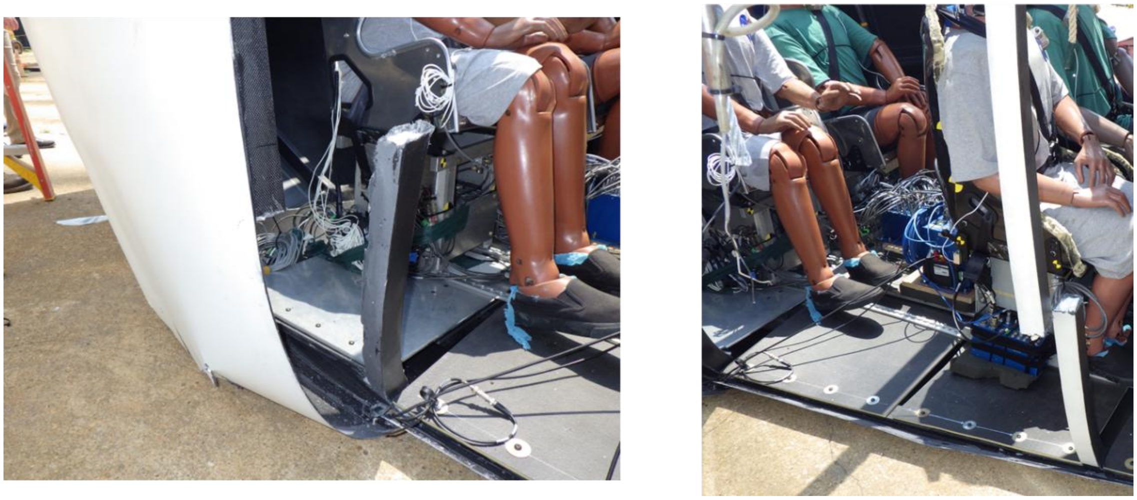

Figure 17. Starboard side C- (left) and B- (right) pillars

The interior of the test article is next shown examining the split that occurred aft of the rear rows of seats. This image of the split, which is depicted next in Figure 18, is taken from a view looking forward from the tail of the test article.

Figure 18. Aft Section split

Next, the seats and floors were removed to inspect the performance of the subfloors. Inspections of the post-test subfloor EA components revealed uneven crushing from the test. The front EA subfloor, which is on the left in Figure 19, is essentially uncrushed in the front and slightly crushed on the rear starboard side. This EA subfloor was in front of the front seats, and the only items of mass directly over it was the front row ATD feet. The starboard side crush is a result of the H3 95th ATD in Seat 1, whereas the port side Seat 2 contained the smaller H3 5th ATD. The EA subfloors in the row which contained Seats 1 and 2, showed large differences in crush displacement. The largest displacement was under Seat 1, which contained the largest H3 95th ATD. Thus, the added weight of this ATD enabled the almost complete crush of the EA subfloor. Seat 2, which contained the H3 5th ATD, showed signs of uneven crush, with the starboard side showing greater crush displacement than the port side. This could be due to the ATD having the lightest mass, but also due to the roll and yaw from the impact. From the aircraft reference point, the lateral motion of the ATDs would be primarily in the starboard direction at impact, and thus uneven crush of the EA subfloor would be directly affected by this motion. The crushed EA subfloors are shown in Figure 19.

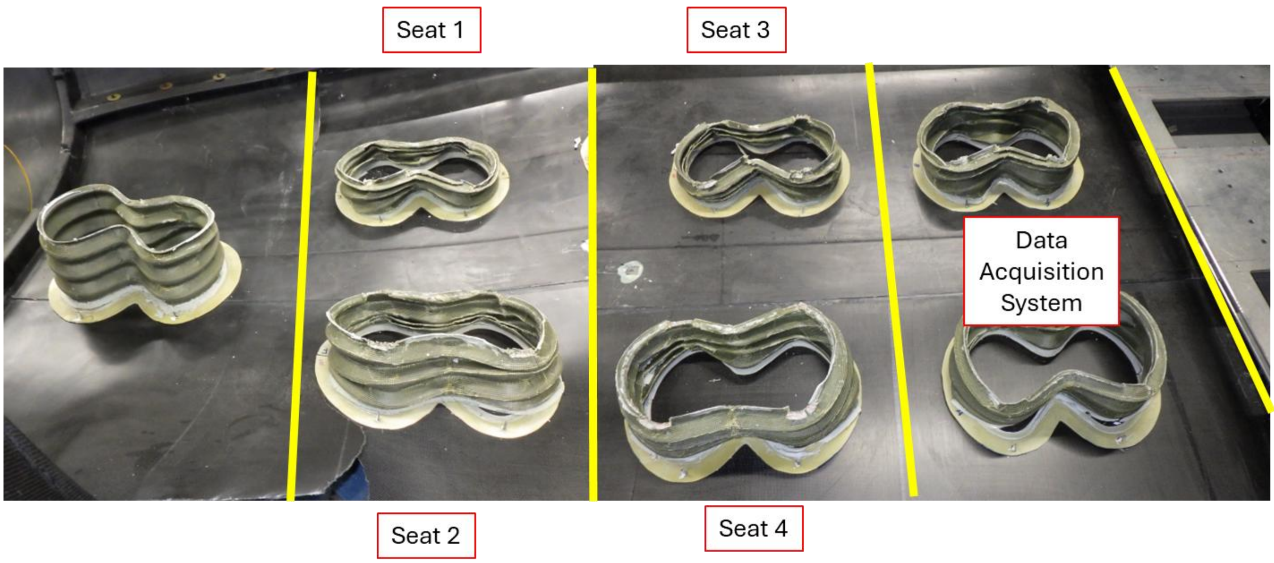

Figure 19. Post-test EA subfloors

The second row of seats, which consisted of Seats 3 and 4, showed more uniform crush both between the two seats and also within the EA symmetry itself. Seat 3, which was the rigid seat, appeared to show more crush displacement than Seat 4 which was a NASA EA seat. However, both showed signs of an almost complete crush displacement after impact. The DAS EA subfloors also appeared to crush to some extent, however, since they did not affect any of the ATD results, they were not investigated further. Several measurements were made of the EA subfloor crush immediately post-test, by using the gaps in the floors to measure the distance between the belly and the top of the floor. An example of this measurement is shown for the H3 5th ATD in Seat 2 in Figure 20.

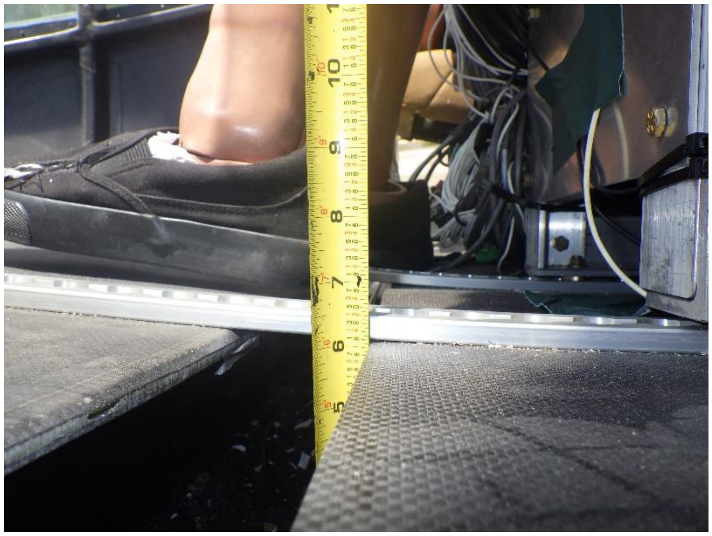

Figure 20. Subfloor post-test measurements

This is only an indirect measurement since the subfloor was essentially in the middle of each floor panel, but also the only way to obtain crush response prior to test article disassembly. It should be also noted these measurements would not show the maximum crush of the EA subfloor since the maximum crush occurred during the test and the EAs subsequently rebounded post-impact. These measurements are shown in Table 3.

Table 3. Post-test subfloor crush displacement

Seat #	Measurement location	Crush displacement (inch)
1	Forward floor	5 ½
2	Forward floor	2
3	Forward floor	5 ¾
4	Forward floor	2 7/8

Airframe Accelerations

After the visual inspections of the test article were complete, the DAS data was examined to determine the levels of loading that occurred in the various locations in the airframe and ATDs. A sampling of accelerometers measuring the horizontal accelerations in various portions in the test article are shown first in Figure 21. Unless specifically noted, all acceleration data is filtered in accordance to SAE J211 filtering schemes [19].

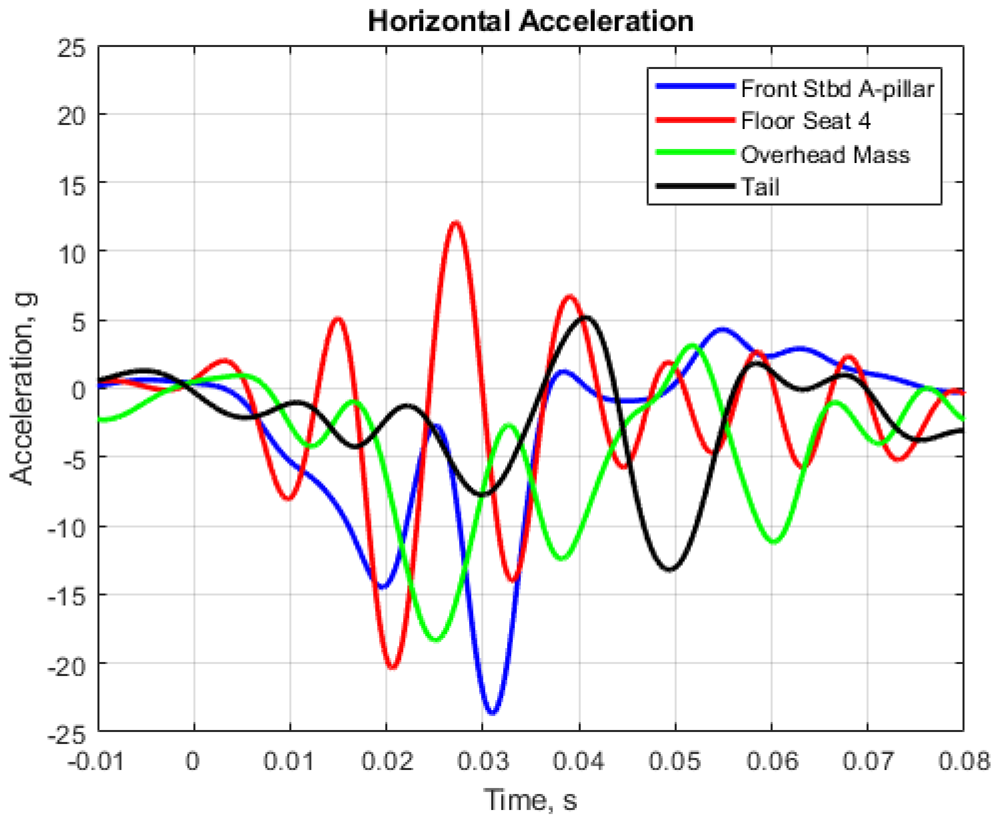

Figure 21. Test article horizontal acceleration

The accelerometer data presented in Figure 21 are a sampling from different parts of the test article, including the front frame, floor, overhead mass and tail. The acceleration data was oscillatory in nature but resembled a triangular-to-trapezoidal pulse shape, with peak values occurring between 20 g and 23 g, depending on the location. The overall acceleration pulse shapes for areas around the cabin were all similar in nature both in shape and duration indicating that, in general, the test article experienced nearly uniform horizontal response during the impact event. However, the tail showed a less severe pulse shape, with lower magnitudes and a spike that occurred later in the time history. The reduction in horizontal acceleration in the tail section is indicative of the energy absorbed through the vehicle structure from the impacting surface under the vehicle body to the tail section which was not in contact with the ground. Since the test article impacted with a nose-left yaw, the impact event produced three-dimensional loading in the test article. The lateral acceleration data are next shown in Figure 22.

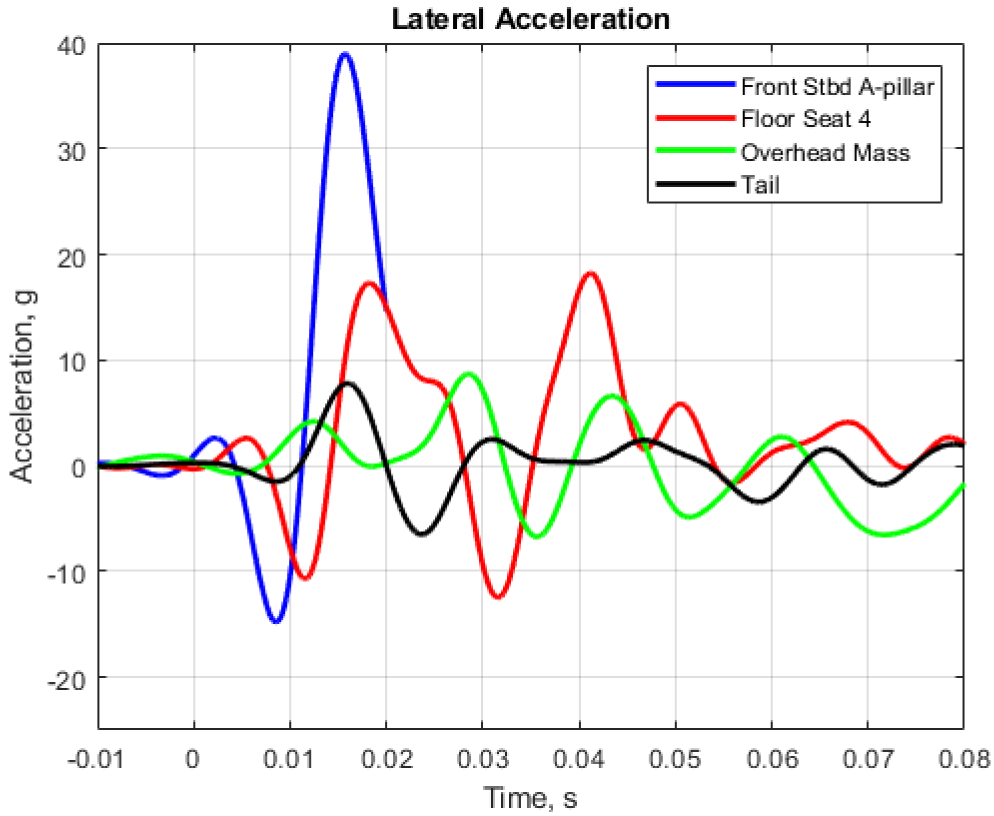

Figure 22. Test article lateral acceleration

There was a large spike in the acceleration levels in the front starboard A-pillar, which is expected since the starboard side was the location of the initial impact. The acceleration spiked to approximately 38.9 g, which attenuated through the floors to a magnitude of approximately 17.3 g at the floor level. It was further attenuated at the overhead mass and tail levels, with peak values of accelerations less than 10 g occurring in those locations. Unlike the horizontal acceleration, which was primarily dominated by the skidding of the full airframe belly, the lateral accelerations were shown to have increased sensitivity to deformations of the airframe relative to the point of initial impact.

Finally, acceleration progression throughout the test article in the vertical direction was examined. The acceleration starting at the belly of the aircraft, base of the A-pillar, over the crushable subfloor, and at the top of the aircraft measured in the overhead mass, are shown in Figure 23.

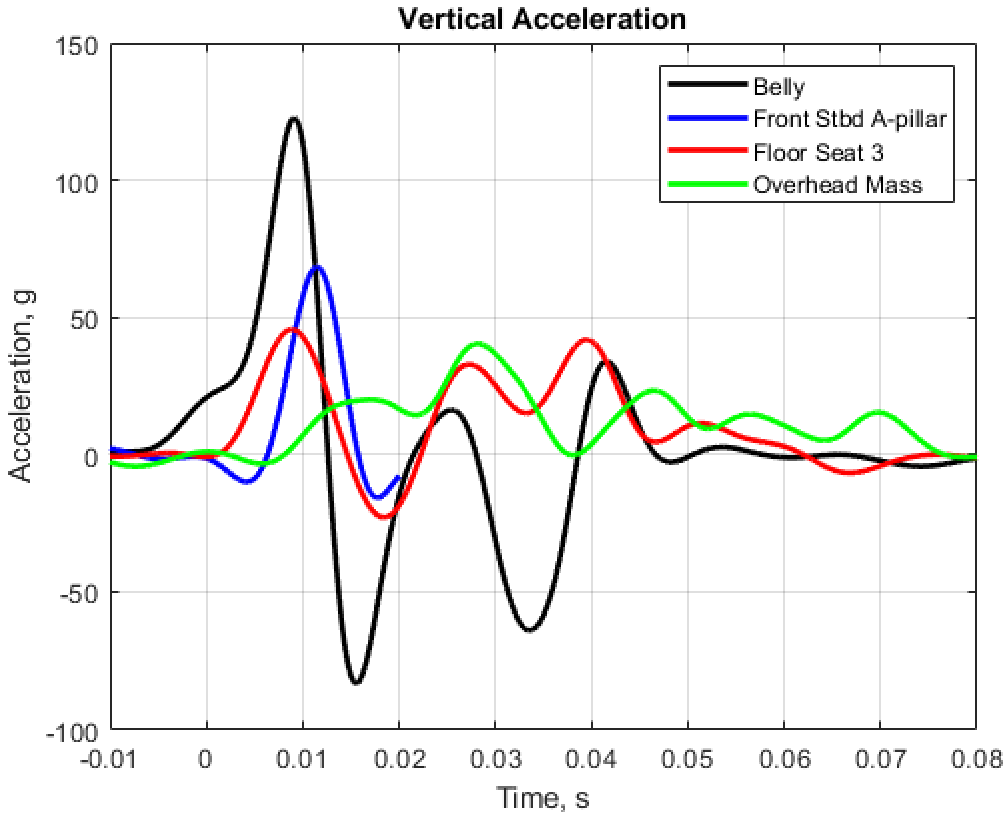

Figure 23. Vertical acceleration progression through the floor

Max accelerations were 122 g for the belly, which represented the base of the test article impacting the impact surface. This acceleration was attenuated to 68 g at the front starboard A-pillar and further down to 45.4 g at the floor level, which is represented in the plot by the Seat 3 trace. The vertical acceleration was attenuated further when examining the overhead mass results, noting a peak magnitude of 40.3 g, which occurred approximately 0.028 s after impact. The belly acceleration did not have a defined shape but was more of a single spike/peak value which occurred immediately after impact. The floor acceleration resembled a trapezoidal shape but included a dip in the middle of the loading condition at approximately 0.018 s after impact. The decrease in peak acceleration, as impact force moved upwards through the airframe, is produced by the energy absorption within the vehicle structure as it deforms downward during impact. Note that the front starboard accelerometer on the A-pillar is only plotted to 0.02 s after impact, and thus a pulse shape cannot be defined. The data was deemed unreliable due to sensor issues that occurred after this point in time.

Next, accelerations at the rear ESS ballast locations were examined. The acceleration results from the port side ESS ballast utilizing several filtering schemes are shown in Figure 24.

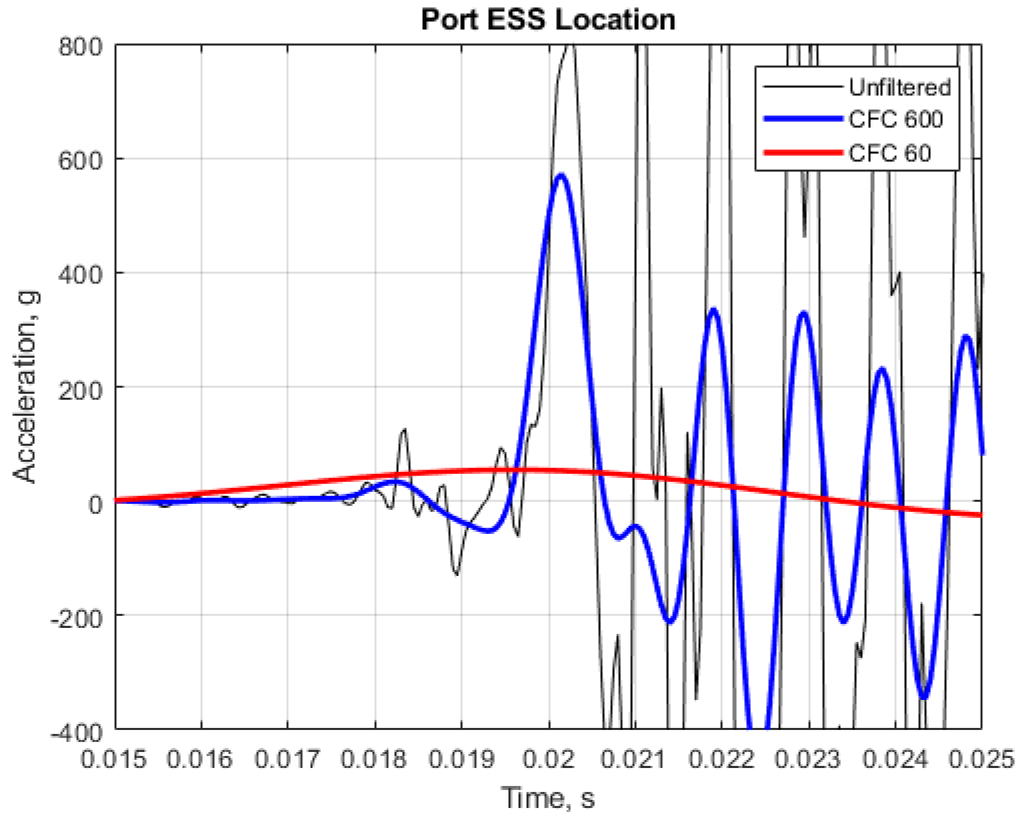

Figure 24. Port side ESS location response filtered at various CFC filter levels

The results obtained in the ESS ballast were similar in nature to those obtained from the Phase 1 ESS component level drop testing [16]. A high magnitude, low duration spike recorded in the accelerometers led to the formulation of a shock type of event, rather than a typical pulse within the crash family. Similar to what was examined on the data collected at the ESS component level, several different filtering schemes were attempted to best quantify acceleration response in the ESS ballast. Channel Frequency Class (CFC) 60 and CFC 600 are two different filtering schemes called out in SAE J211 that were utilized for this process. The first CFC 60 filter was utilized by examining the data as a total vehicle acceleration. This is the common filter used when examining structural response from tests and data presented are primarily filtered with this filter. The other filter investigated was the CFC 600, which is called out as a component analysis filter, which this ESS structure could be considered. The CFC 600 filter removed the high spikes, and had a peak acceleration value of approximately 571 g, for a duration of approximately 0.001 s. These parameters are of similar magnitude and duration as the data collected from the ESS component level drop test. The CFC 60 filter appeared to flatten out the original signal in a way which changed the overall response, giving a peak acceleration value of only approximately 54.7 g, for a duration of approximately 9 ms. The data acquired from the ESS ballast is important to study, because the filtering used can drastically change the results, and thus should be interpreted carefully. This effect on the floor level accelerations is next shown in Figure 25.

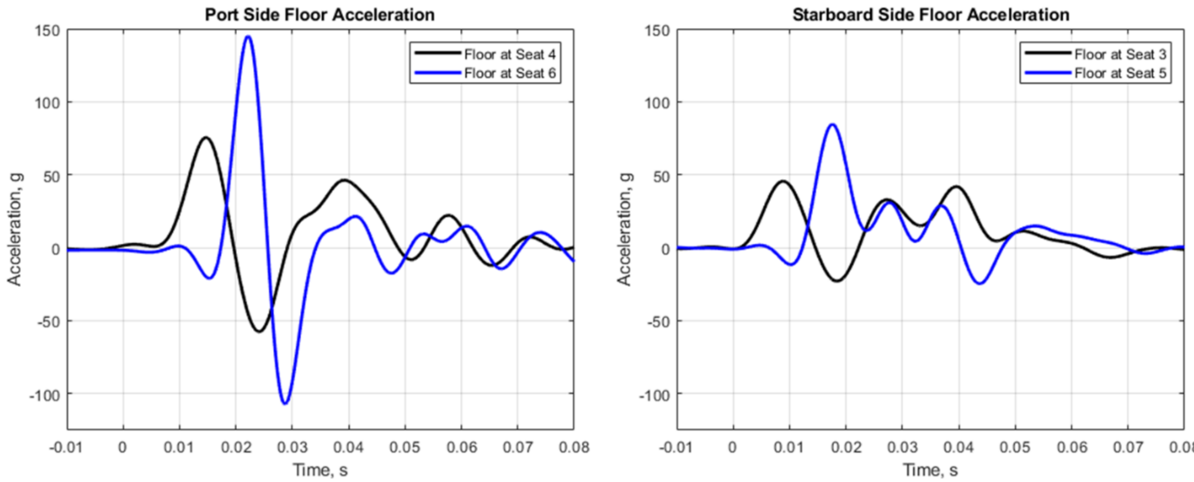

Figure 25. Accelerations compared between floor regions on EA subfloor (3&4) and on the ESS structure (5&6)

On the port side, the floor above the ESS and below the NASA EA seat (Seat 6) experienced approximately 145 g, while the floor in front of it in the middle row over an EA subfloor (Seat 4) experienced a 75 g peak acceleration, representing a 48% reduction. On the starboard side, the floor above the ESS and below the rigid seat (Seat 5) experienced 84 g, while the floor in front above an EA subfloor (Seat 3) was approximately 45 g, representing a 47% reduction in accelerations at the floor level.

Photogrammetry Results

The individual bowtie targets were tracked throughout the time-history of the event, including the swing, impact and subsequent deformation and vehicle slide out. Typical marker tracking analysis is shown in Figure 26. Using the port-side camera system, the vertical and horizontal velocities, as well as the pitch angle, were calculated by tracking the bowties that were positioned on the lifting hardware. The East-view camera system was positioned to view the tail of the vehicle, which provided the vertical velocity and the roll angles, as shown in Figure 27. The yaw angle was measured and calculated using a combination of the East-view (tail) and West-view (nose) camera systems, along with the centerline of the LandIR facility.

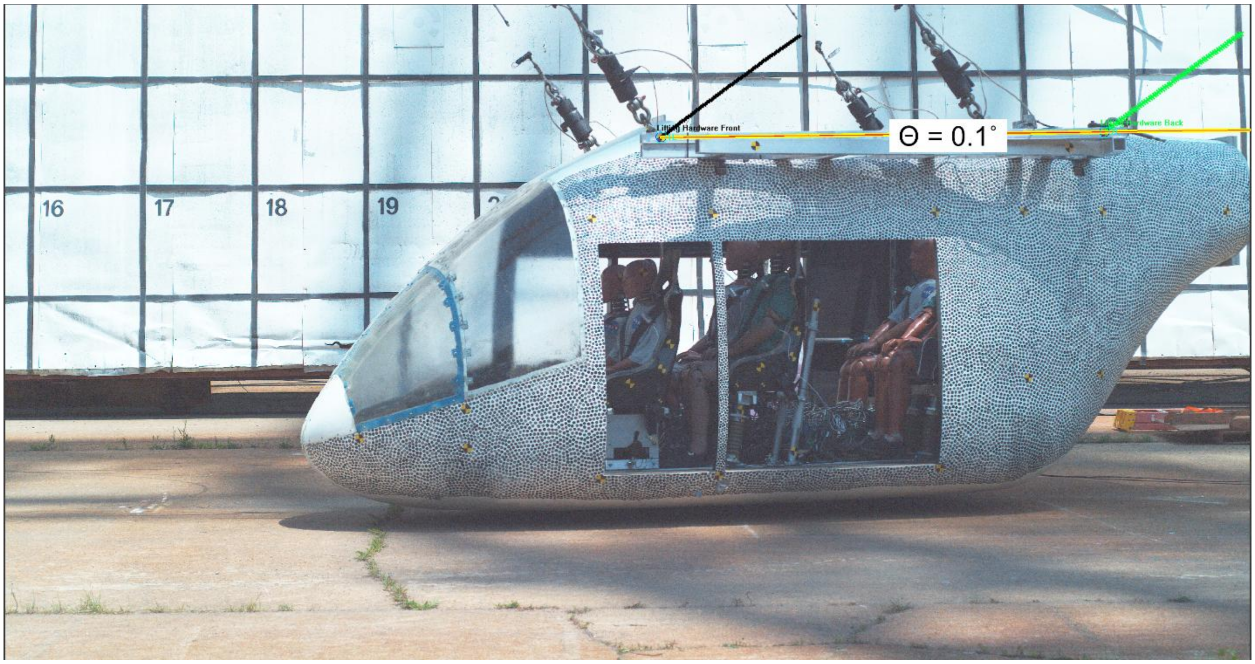

Figure 26. South (port-side) view showing pitch angle at impact

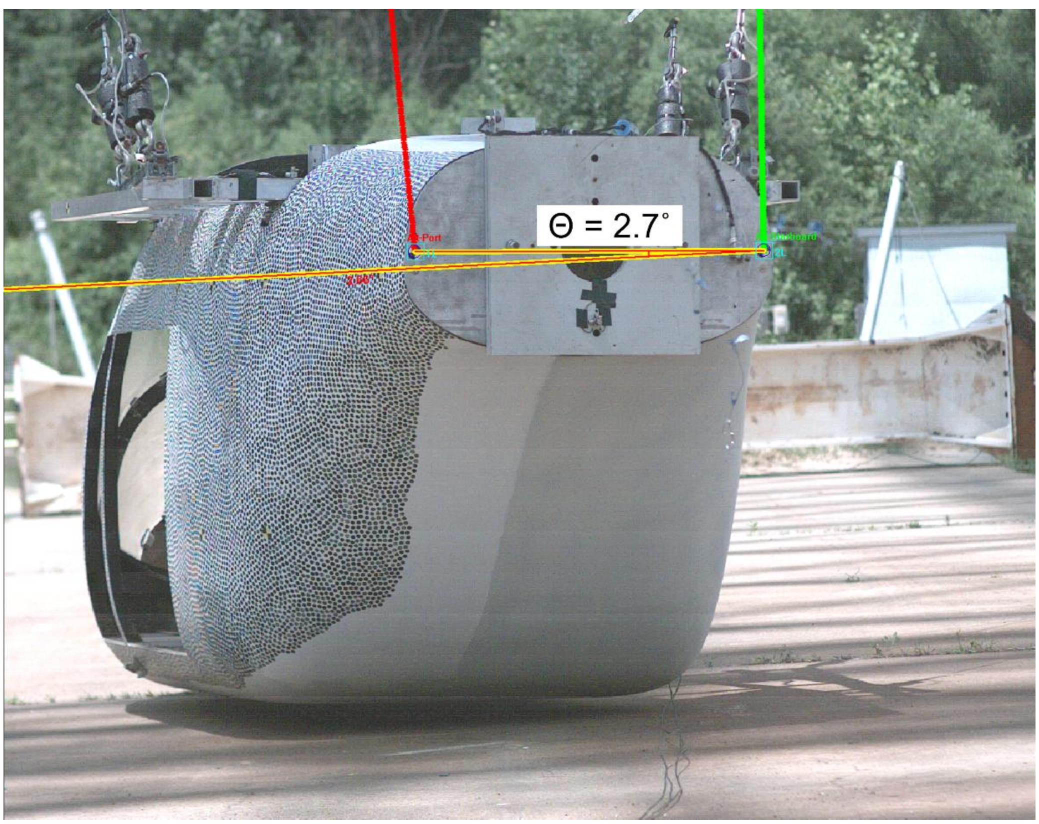

Figure 27. East (tail) view showing roll angle at impact

The 3D-DIC results are shown next in Figure 28 through Figure 33. The vertical and out-of-plane displacement contour plots are shown in Figure 28 and Figure 29, respectively. The full-field contour image sequence follows the notable event timing listed above in Table 2. Note, due to the large amount of displacement observed, the range of the contour scale changes throughout the image sequence. The purple color represents the minimum value, while the red color represents the maximum value.

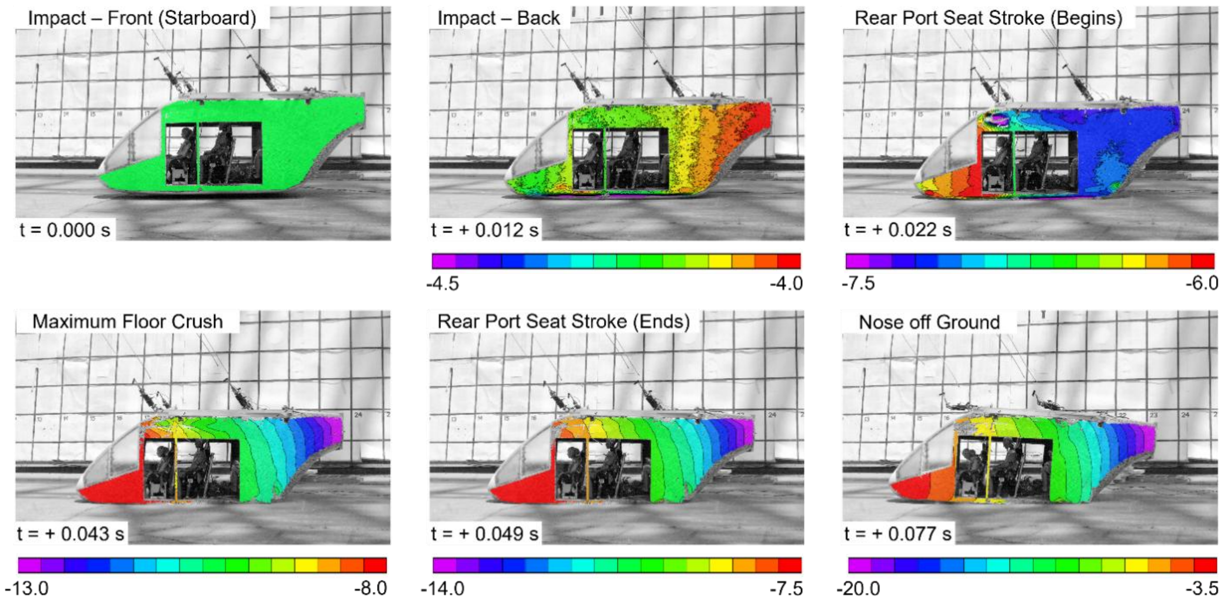

Figure 28. Port-side vertical deformation contour plots, in inches

The upper left image in Figure 28 shows the test article at impact. Following impact, extensive crushing occurred in the belly of the test article, as shown in the upper middle image and denoted by the purple contour, which is also the time the C-pillar impacted the ground. During this time, the vertical deformation of the test article is uniform, which is evident by the uniform vertical contour gradient levels and overall contour scale. At approximately 0.022 s after impact, Seat 6 began to stroke, and larger deformations were observed in the rear section of the vehicle. Between 0.022 s and 0.077 s, the subfloor reached maximum compression (lower left image) and the forward section of the vehicle began to rotate to a nose-up pitch. At 0.077 s after impact, the nose of the vehicle rotated off the ground, and the tail section rotated downward to approximately 20 in. below the initial impact position. Out-of-plane deformation is next shown in Figure 29.

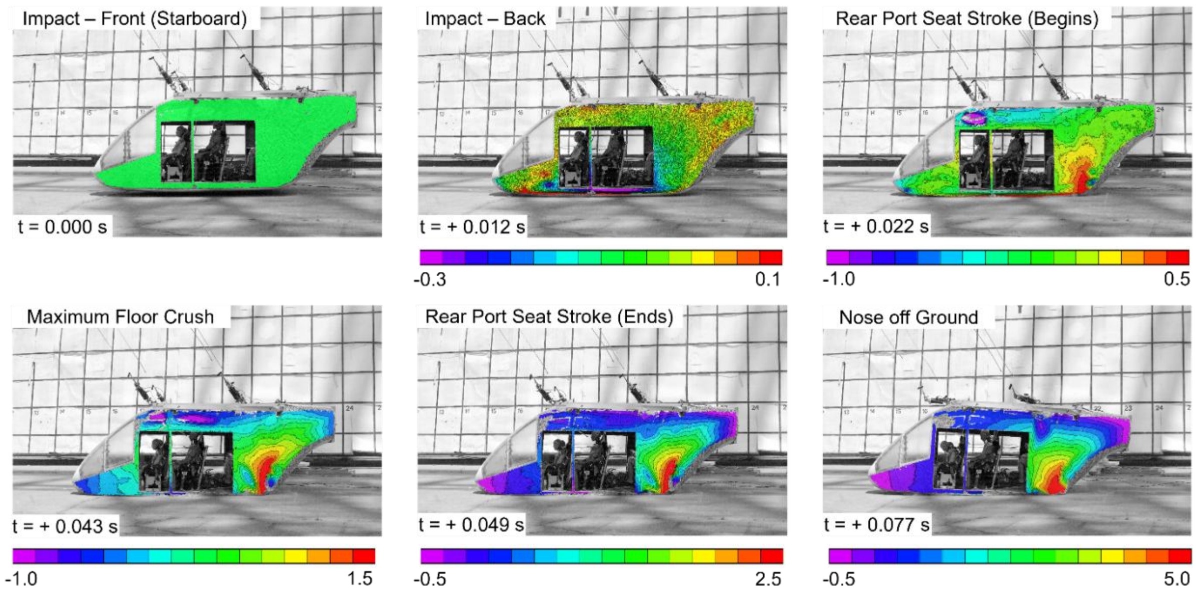

Figure 29. Port-side out-of-plane deformation contour plots, in inches

By 0.022 s after impact, extensive crushing in the belly occurred by noting the red and purple contours which began to develop at 0.012 s. This event is shown in the upper middle image, which is followed by localized buckling in the forward and aft section of the fuselage, which is shown in the upper right image. There is inward buckling in the forward section above the cabin, shown in purple and outward buckling in the aft section behind the C-pillar, which is shown in red. Localized buckling continued to develop, as shown in the lower left image at 0.043 s, and damage is evident in the fuselage behind the C-pillar. The out-of-plane deformation continued to grow, and by 0.077 s, the deformation reached approximately 5 in. These structural deformations were further interrogated utilizing virtual extensometers created by the 3D-DIC system. These extensometers are next shown in Figure 30.

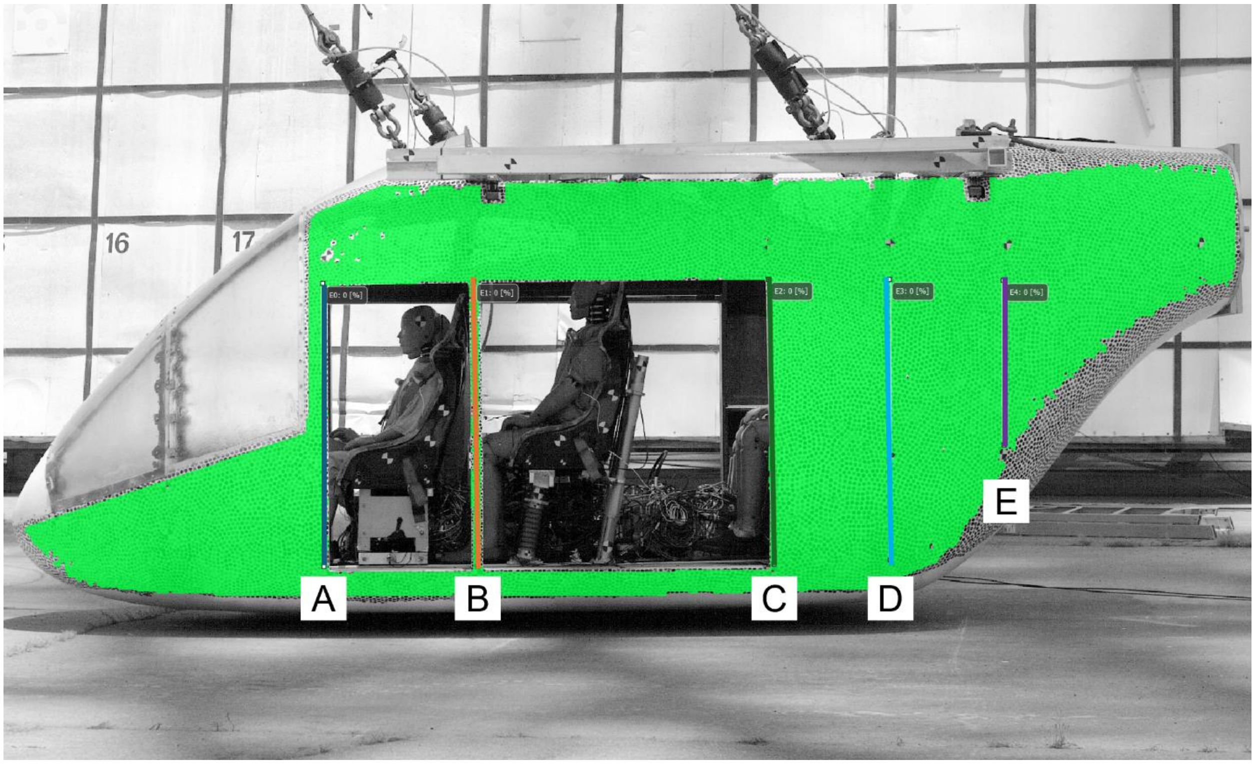

Figure 30. Port-side virtual extensometer locations on airframe pillars

Virtual extensometers were positioned on five of the airframe pillars, as shown in Figure 30. The virtual extensometers positioned on A-pillar through D-pillar were approximately 48 in. long, while the virtual extensometer positioned on the E-pillar was approximately 36 in. long. The virtual extensometer time-history plot for all pillars is shown in Figure 31.

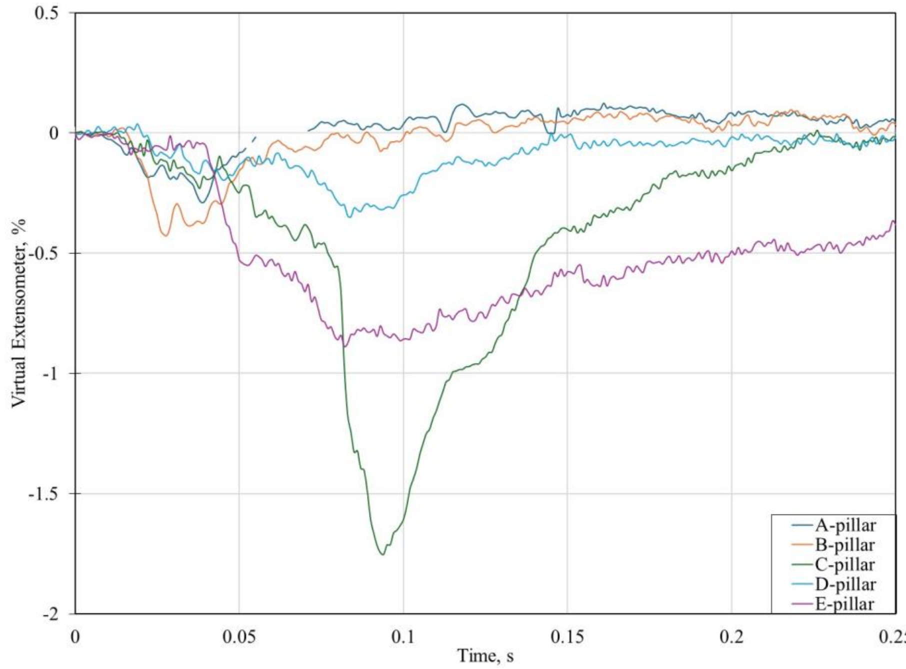

Figure 31. Time-history of virtual extensometer locations on airframe pillars

As shown in Figure 31, the C-pillar exhibited the largest amount of compressive strain of approximately 1.75%, which occurred approximately 0.09 s after impact. This large spike in compressive strain was followed by a rapid reduction in strain over the next 0.15 seconds. This result led to further examination of the high-speed data, with a primary focus on the C-pillar. Further inspections revealed that a crack formed in the C-pillar at 0.091 seconds after impact due to the compression of the vehicle during impact and the subsequent outward bending This crack is highlighted in Figure 32.

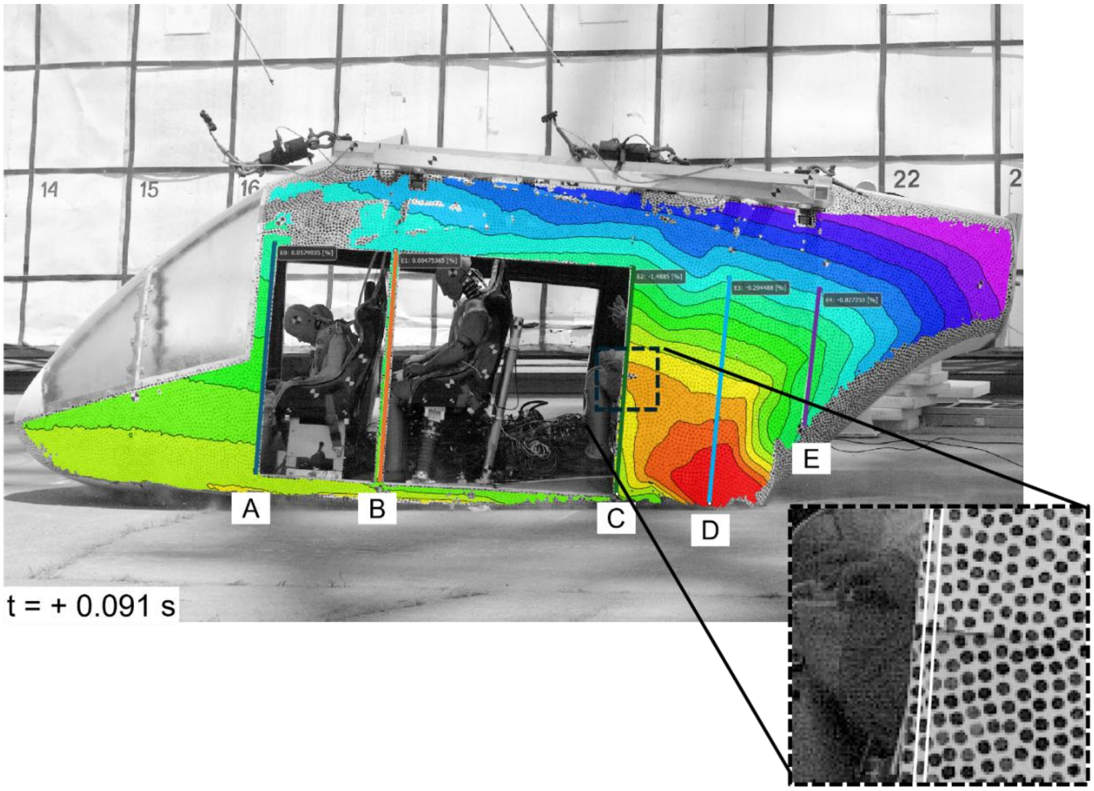

Figure 32. Port-side C-pillar failure

This failure response is also highlighted in Figure 33, which shows the maximum principal strain contour plots for a previously conducted component level drop tower test [12] in Figure 33, left, and the full-scale L+ C #2 test in Figure 33, right. In both tests, the maximum principal strain reached approximately 1.6% prior to a tensile crack forming on the outermost surface, which provided evidence that this strain level was the material failure in both instances.

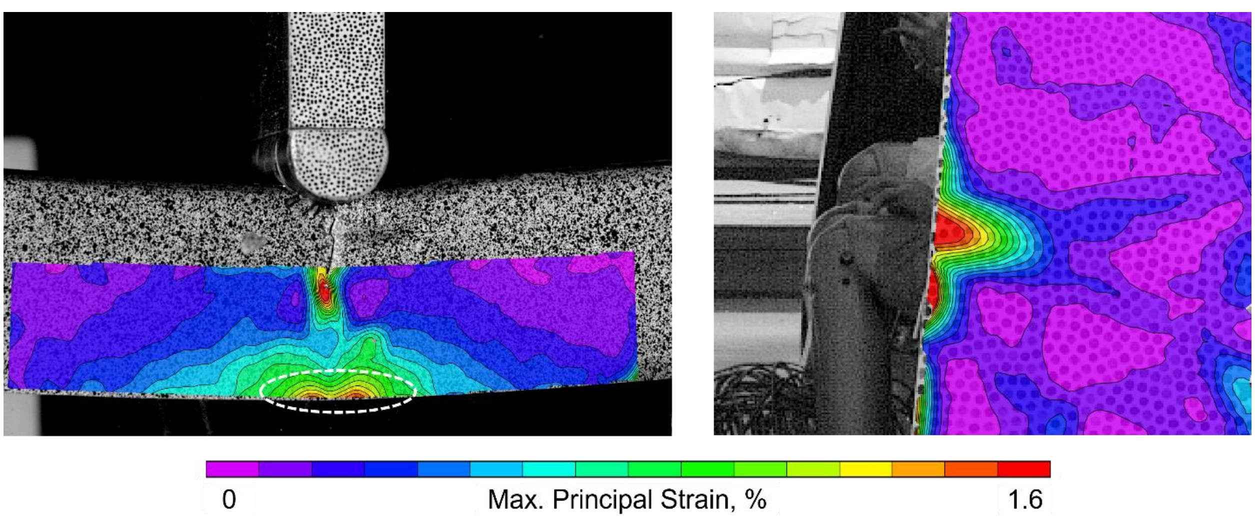

Figure 33. Port-side C-pillar maximum principal strain prior to failure, dynamic 3-point bend (left) and L+C #2 swing test

Seat Performance

After the airframe results were examined, attention was turned to examining the responses of the seats located in the cabin of the test article. Seat 1 contained the H3 95th ATD in the COTS seat with EA subfloor. This seat design was certified to 14 CFR § 27 requirements and featured internal stroking mechanisms. In this test, the seat stroked approximately 2.4 in. and when further examining the Seat 1 data, the floor and the seat pan experienced similar acceleration magnitudes during the initial acceleration spike and the acceleration shape are similar throughout the impact event, as shown in Figure 34, left. Similar initial peak acceleration between the seat and subfloor indicated strong coupling between the seat and floor. The activation of the stroking mechanism resulted in the decoupling of accelerations during the second acceleration spike which occurred approximately 0.025 s after impact. In this second spike, the seat acceleration was reduced relative to the floor. There was the same EA subfloor under Seat 2 however it did not contain any stroking mechanism between the floor and seat pan due to it being a rigid seat. For Seat 2, as shown on the right in Figure 34, the acceleration magnitude and profile of the seat pan matched closely with the floor throughout the impact event. This coupled acceleration confirmed the connection between floor and seat pan remained rigid throughout the impact event. Although Seat 2 did not have a stroking mechanism, the peak acceleration measured was slightly lower than that in Seat 1, which is thought to be from the impact conditions of the test.

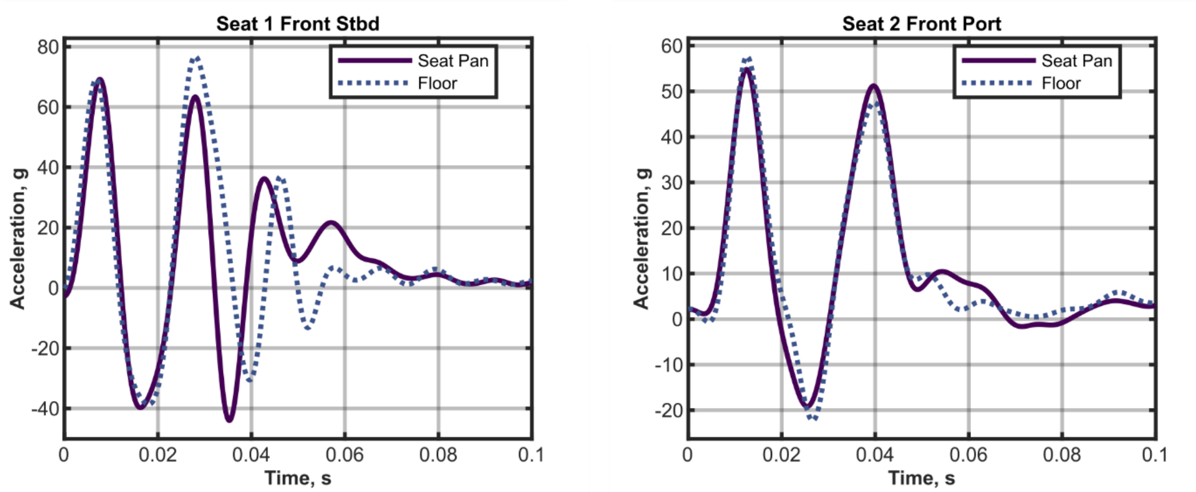

Figure 34. Acceleration of the seat pan and floor for Seat 1 front starboard (left) and Seat 2 front port (right).

The middle row of seats is next examined. Seat 3 and Seat 4 both contained the FAA H3 50th ATD and both had EA subfloors. The acceleration profiles of the seat and floor closely matched for Seat 3, indicating rigidity from the aluminum legs used was maintained throughout the impact event. The acceleration profiles of the seat and floor show clear divergence in Seat 4. Seat 4 was a NASA EA seat which was designed to stroke using sliding rails for the rear supports. These sliding rails decoupled the seat mass from the floor during the vehicle drop and subsequent impact. The large discrepancy between seat pan and floor observed on the initial acceleration spike can be attributed to the decoupling of the seat and occupant mass from the floor, which effectively reduces mass at the measured floor location on initial impact resulting in a high spike in floor acceleration. Although the seat decoupling resulted in a higher floor acceleration in Seat 4 location, there was no discernable improvement in peak acceleration between Seat 3 and Seat 4. Lack of seat acceleration reduction in Seat 4 was due to the fact the EA mechanism in Seat 4 did not stroke effectively. Two potential sources of the poor EA performance in Seat 4 are hypothesized: (1) the subfloor crushing misaligned the seat legs causing them to bind, (2) the impact conditions included a yaw and thus changed the impact orientation and loading into the seat. Seat 3 and Set 4 data are shown in Figure 35.

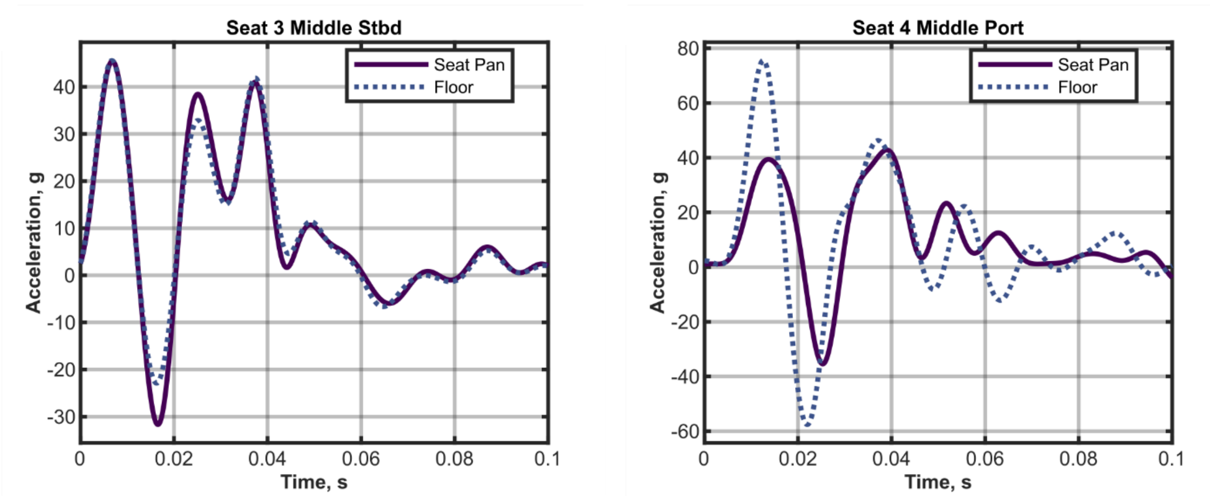

Figure 35. Acceleration of the seat pan and the floor for Seat 3 front starboard (left) and Seat 4 middle port (right).

Seats 5 and 6 differed from the other seats since they were both placed over a rigid subfloor representing the ESS installation. For Seat 6, the seat EA tubes compressed and produced a large stroke as seen in Figure 36, right. For reference, this is compared to the lack of stroke in Seat 4, which is shown in Figure 36, left.

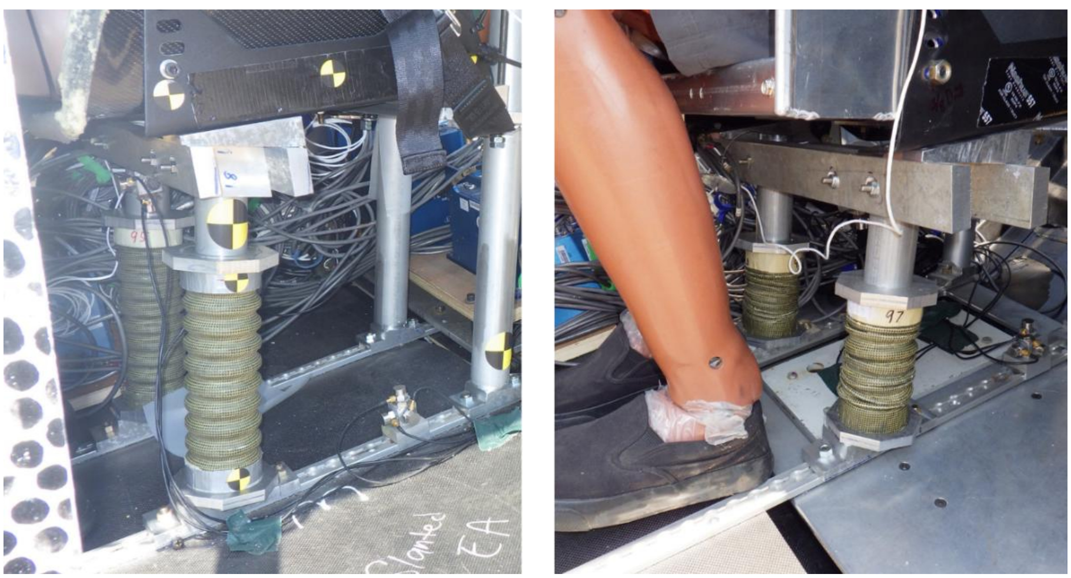

Figure 36. Seat 4 EA tube post-test (left), Seat 6 EA tube post-test (right)

Seat 5 and Seat 6 data are shown in Figure 37 The Seat 5 acceleration magnitudes and profiles are similar between the seat pan and the floor for the same reasons as Seats 2 and 3. Peak acceleration magnitude in the floor was higher under Seat 6 compared to the Seat 5 location, which was attributed to the increase in localized floor acceleration under the seat with decoupled mass as described in Seat 4. Peak acceleration in Seat 6 was reduced relative to Seat 5. Because both seats were on the same rigid subfloor structure this reduction in peak acceleration was attributed to the effectiveness of the energy absorbing capability in the tubes and reducing the energy transferred to the seat pan.

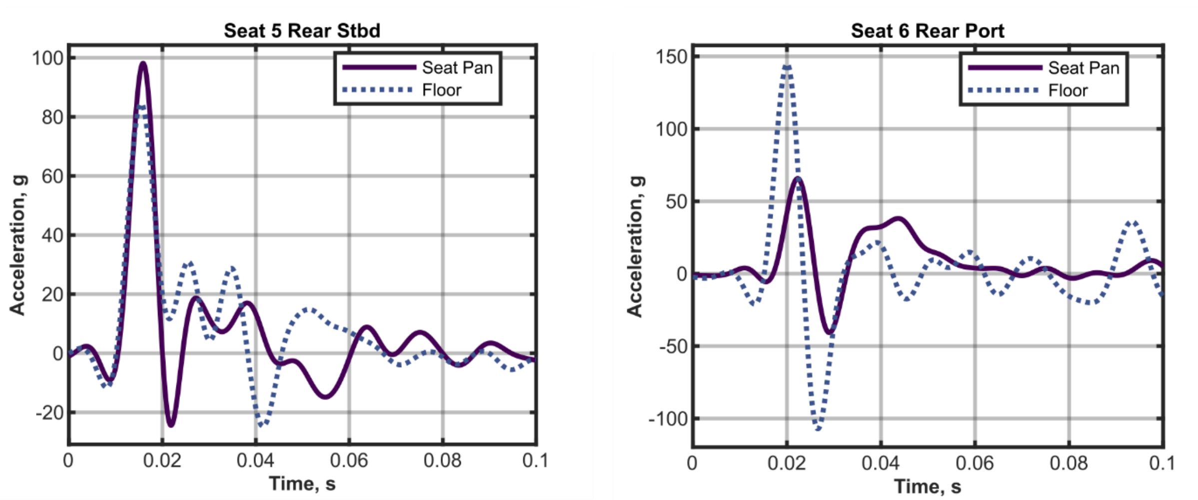

Figure 37 Acceleration of the seat pan and the floor for Seat 5 rear starboard (left) and Seat 6 rear port (right)

ATD Results

Next the ATD results were examined. A summary of the peak values measured from the sensors located in the head, pelvis and lumbar for each ATD is provided in Table 4.

Table 4. Peak acceleration and force measurements at different locations

	Head			**Pelvis**		**Lumbar**	
Location	Ax(g)	Ay(g)	Az(g)	Ax(g)	Az(g)	Fz(lb)	My (in-lb)
Seat 1 – Front Starboard	-12.2	NA	25.0	8.8	22.2	962.0	-761.7
Seat 2 – Front Port	3.4	-11.9	36.6	-9.5	41.2	1203.3	-308.0
Seat 3 – Middle Starboard	0.6	-3.6	31.0	NA	35.1	1852.1	-654.2
Seat 4 – Middle Port	-8.8	1.7	35.6	5.5	40.4	2148.2	344.8
Seat 5 – Rear Starboard	-16.2	NA	96.5	17.1	85.4	3372.3	-2001.1
Seat 6 – Rear Port	-13.3	-3.4	44.4	17.2	40.5	1798.2	-1173.4

The head response time history plots are first shown in Figure 38. The head acceleration measurements are shown for the horizontal (x-direction), lateral (y-direction) and vertical (z-direction) directions are shown in Figure 38A, Figure 38B and Figure 38C, respectively. Head rotations about the y-axis are shown in Figure 38D.

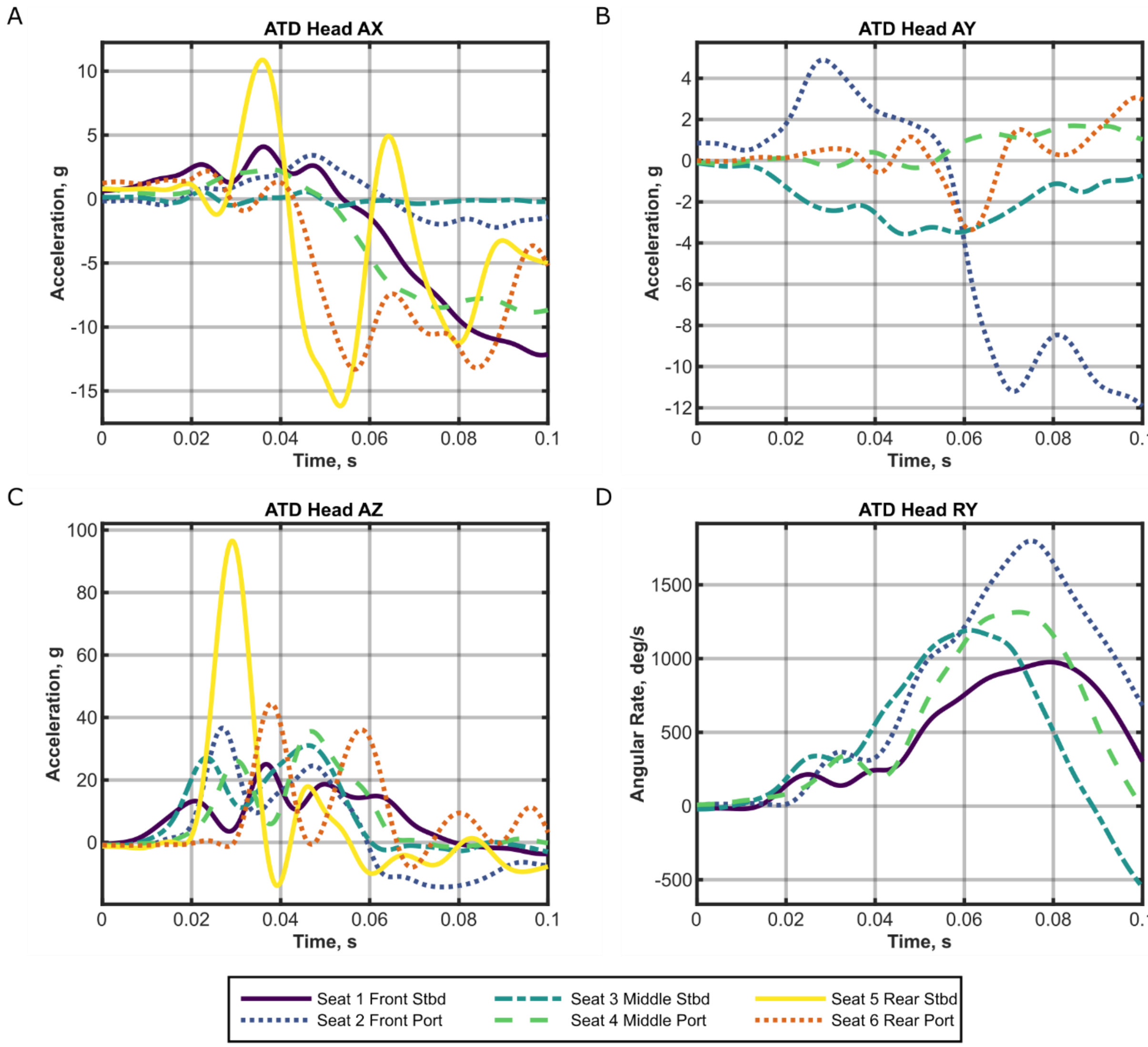

Figure 38. ATD head response: (A) acceleration in horizontal direction, (B) acceleration in lateral direction, (C) acceleration in vertical direction, and (D) head rotation about the y-axis.

For the horizontal direction, there were consistently low magnitudes of acceleration that developed across five of the ATDs. The H2 50th ATD located in Seat 5 showed the highest values in the positive and negative directions. Since this ATD was seated in a rigid seat over a rigid subfloor, along with only having a 3-point seat belt, it was expected the ATD would respond with higher accelerations. The maximum magnitude of accelerations for this ATD were slightly higher than 15 g, which occurred 0.05 s after impact. Shortly after 0.04 s after impact, both H2 50th ATDs in Seats 5 and 6 exhibited similar responses which occurred during the slide out portion of the test. In the lateral direction, maximum values were low in all of the ATDs with the exception of the H3 5th ATD in Seat 2. The Seat 2 ATD head motion began to increase approximately 0.06 s after impact to a magnitude of between 10 g and 12 g. This motion was because of two related factors. The first is the yaw from the test which pulled the ATD out of the seat toward the starboard side of the test article, and the second is due to the small size of the ATD. The shoulder belts were routed to holes in the seat back for all ATDs, and due to the smaller size of the 5th ATD, there was a greater space between the shoulder belt attachment point on the seat and the routing of the belt went over the shoulder. Due to this space, the ATD range of motion was higher than the larger 50^{th} size ATDs. The acceleration values from the H3 95^{th} ATD seated in Seat 1 and the H2 50^{th} ATD seated in Seat 5 were not available due to sensor cabling issues.

As expected, the vertical accelerations exhibited significantly higher peak values. The H2 50^{th} ATD seated in Seat 5 measured approximately 97 g, which was significantly higher than the other ATDs. This response is attributed to its seat location over the rigid floor seated in a rigid seat. The other ATDs maintained acceleration peak levels below 45 g, which demonstrated the effectiveness of the energy absorbing mechanisms in reducing impact loads in the head and the critical impacts of ESS placement. The rotation rates for all ATDs resembled similar response shapes and magnitudes, reaching peak values between 0.06 and 0.08 s after impact. The response of the upper neck is next shown in Figure 39.

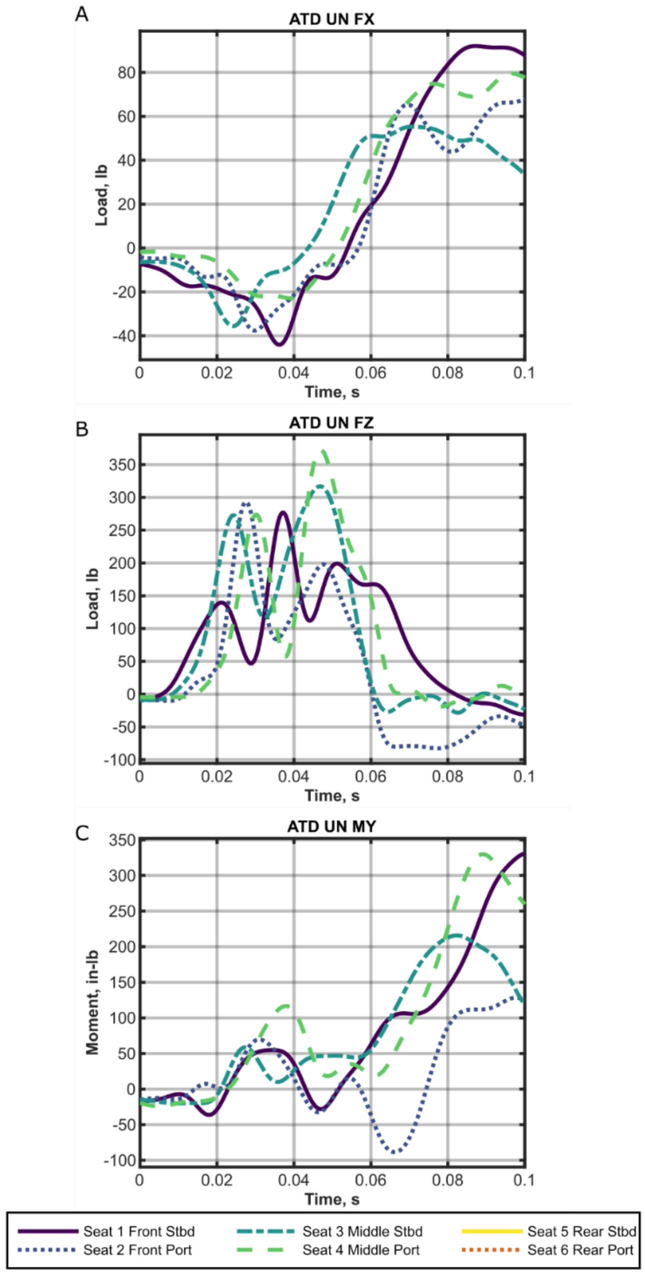

Figure 39. ATD upper neck response (A) load in horizontal direction, (B) load in vertical direction, and (C) moment about the y-axis.

Due to the design of the neck in a H2 ATD, data was not collected for the H2 50th ATDs located in the rear Seats 5 and 6. In the other H3 ATDs where neck loads were collected, overall upper neck response remained consistent amongst all the ATDs. Peak sheer force in the upper neck ranged from approximately 50 lb. to 90 lb., while vertical force in the neck was primarily compressive and peaked between 250 lb. and 400 lb. Upper neck moment was primarily in flexion and had the widest range in peak value, ranging from approximately 150 in-lb to 350 in-lb.

To evaluate the probability of injury using the head and upper neck data, two different criteria are used. The first is the head injury criterion (HIC) which utilizes the collected ATD head accelerations and is based on the following equation [20]:

$$HIC = \max\left\{\left[\frac{1}{t_2-t_1}\int_{t_1}^{t_2} a(t)dt\right]^{2.5} * (t_2 - t_1)\right\} \quad (1)$$

The requirement for this criterion is that HIC must not exceed 700. From Table 5, all HIC values remained under 700. All of the ATDs had similar HIC values, except for Seat 5 which was over 7 times larger than the rest. This is believed to be due to the ATD being placed over the rigid floor which did not contain EA mechanisms. The second criterion is the neck injury criterion (Nij) which utilizes the collected neck forces and moments and is based on the following equation [20]:

$$N_{ij} = \left[\frac{F_z}{F_{int}}\right] + \left[\frac{M_y}{M_{int}}\right] \quad (2)$$

The neck injury criterion takes into account both load and moment. F_z and M_y are the maximum load and moment transformed to the occipital condyle location and taken at the same point in time. F_{int} and M_{int} are the critical intercept load and moment defined by standards for specific occupant sizes. The limit for Nij used for aerospace injury risk calculation was 0.5. As shown in Table 5, all the ATDs remained below the 0.5 limit. Values were not calculated for the H2 50th ATDs.

Table 5: Head impact condition (HIC) and neck injury criteria (Nij)

Location	**HIC**	**Nij**
Seat 1 – Front Starboard	18.90	0.24
Seat 2 – Front Port	41.22	0.40
Seat 3 – Middle Starboard	57.92	0.29
Seat 4 – Middle Port	63.54	0.37
Seat 5 – Rear Starboard	486.12	Not Calculated
Seat 6 – Rear Port	66.44	Not Calculated

Next, the chest response was examined. It is plotted for all ATDs at all locations in Figure 40.

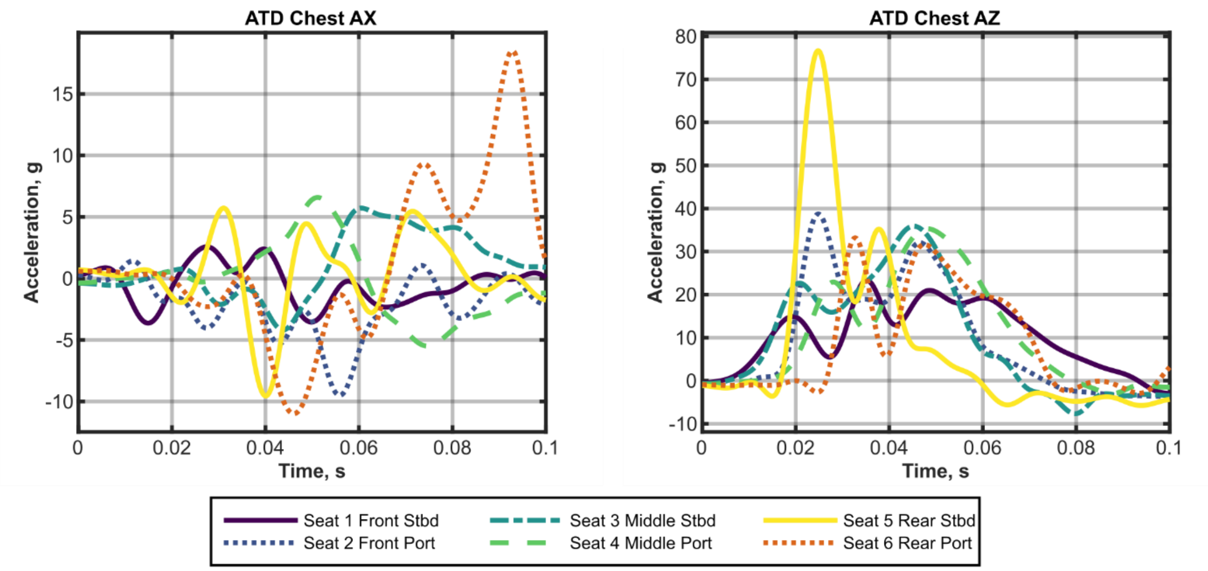

Figure 40. ATD chest response acceleration in horizontal direction (left) and acceleration in vertical direction (right)

The acceleration in the forward direction remained low with the values reaching magnitudes of approximately 10 g which occurred starting at approximately 0.04 s after impact. These results mimicked what was measured in the head and primarily resultant from the slide out post-impact. Ther was a large spike above 15 g that occurred in the H2 50th ATD seated in Seat 6 after approximately 0.09 s. This spike in positive chest acceleration is indicative of the seat striking the back of the ATD.

In the vertical direction, the most significant response is from the H2 50th ATD seated in Seat 5. This ATD experienced a significantly larger peak value of 77 g compared to the remaining ATDs which were below 40 g. The high g levels in the chest mimic those seen in the head for this ATD at this seat. Next the lumbar loads were examined. They are shown in Figure 41.

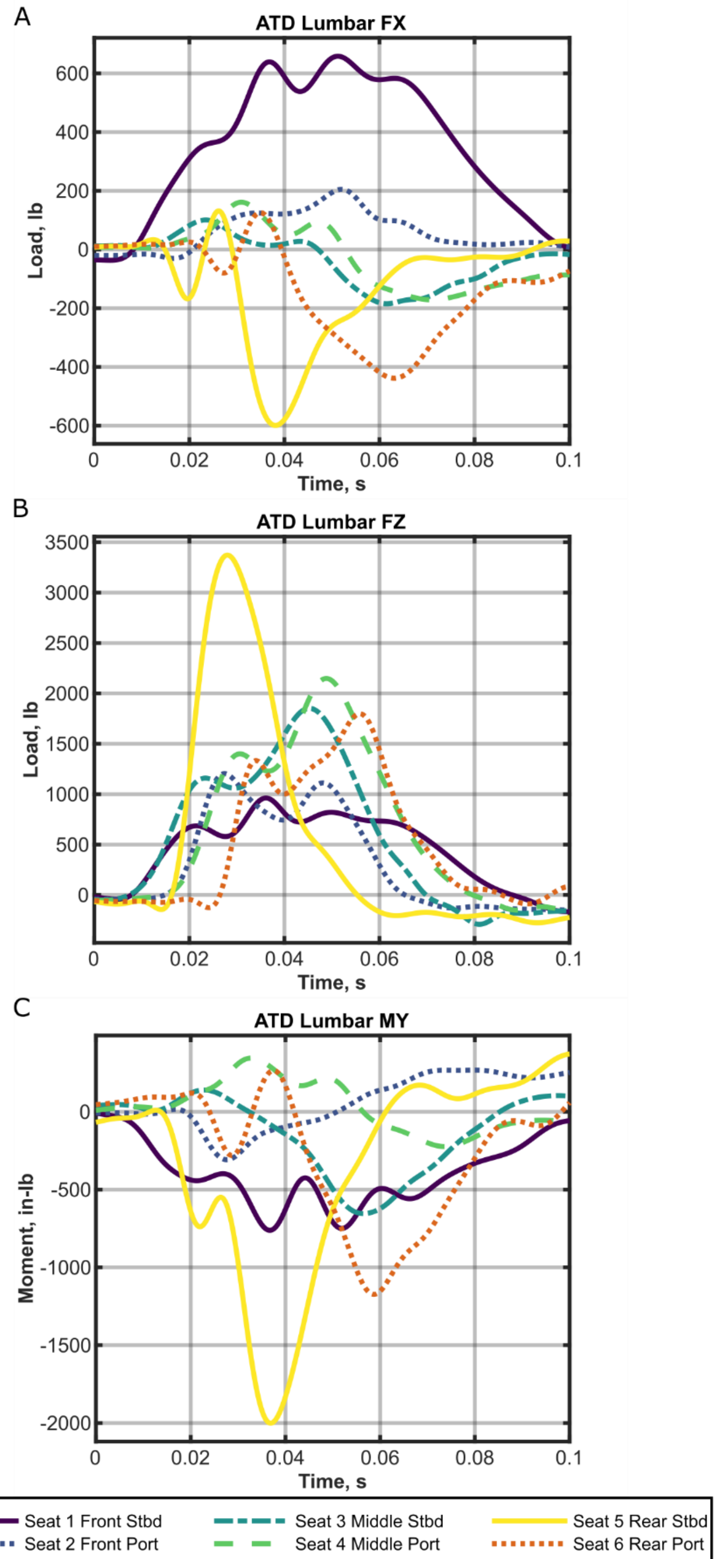

Figure 41. ATD lumbar response (A) load in horizontal direction, (B) load in vertical direction, and (C) moment about lateral direction

In all of the ATDs, the lumbar load in the horizontal direction is significantly lower than the vertical direction. Utilizing current FAA regulations [11], the maximum lumbar load must not exceed 1,500 lb. for a 50th percentile ATD in order to be within certification limits. These values are scaled to encompass other sized ATDs, and criteria developed according to [20], allow for 933 lb. for the H3 5th ATD, and 1,757 lb. for the H3 95th ATD. The data collected from the test showed only one of the ATDs produced a response meeting these criteria. The H3 95th ATD seated in Seat 1 measured a load of 962 lb., which was significantly less than the criteria of 1,757 lb. This ATD was in a COTS seat which both stroked during the test and was placed above the EA subfloor which also crushed to produce conditions to effectively reduce the lumbar load. Seats 2-4 and Seat 6 were all over the criteria, which ranged between 120% and 143% of the limit value, while Seat 5 was 225% over the limit value. Seat 5, due to its location in the rear starboard over the rigid subfloor, was expected to produce lumbar forces higher than the other ATDs due to these conditions.

For reference, The L+C #1 test contained two seats that were below the certification limit values. These two seats were EA seats that were positioned above an EA subfloor. For this test, only one seat - Seat 4 - had a similar condition. However, the seat EA tubes did not compress during impact as intended, and thus the energy that would have been absorbed by the EA tubes was absorbed by the ATD instead, resulting in a larger lumber force. Overall, these results demonstrate the need for the EA subfloor and the seats to work as a system to effectively reduce lumbar loads to within the acceptable values. A summary of the lumbar load peak values and their comparison to the limit values is shown in Table 6.

Table 6: Lumbar Load Criteria

Location	**Fz (lb)**	**Limit Value (lb)**	**Percentage over (%)**
Seat 1 – Front Starboard	962.0	1757	55
Seat 2 – Front Port	1,203.3	933	129
Seat 3 – Middle Starboard	1,852.1	1,500	123
Seat 4 – Middle Port	2,148.2	1,500	143
Seat 5 – Rear Starboard	3,372.3	1,500	225
Seat 6 – Rear Port	1,798.2	1,500	120

Finally, the pelvis results are shown in Figure 42. The acceleration in the horizontal direction remained small in reaching between -10 g and approximately 17 g for all ATDs. As with the head and chest data, the acceleration in the vertical direction measured significantly larger magnitudes. Once again, the H2 50th ATD seated in Seat 5 had a significantly larger magnitude of acceleration of approximately 85 g, which was approximately double the peak magnitudes of the remaining ATDs. Also, it should be noted that the middle starboard acceleration data in the horizontal direction is omitted because the data was compromised by apparent instrumentation issues, likely attributable to sensor or cable failure.

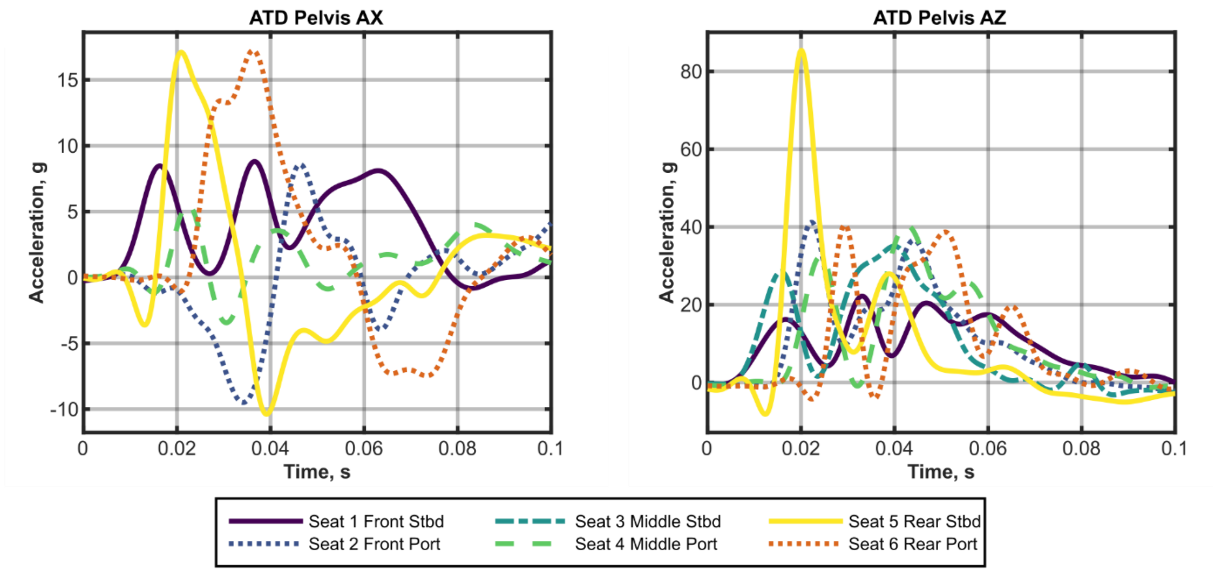

Figure 42. ATD pelvis response acceleration in horizontal direction (left) and acceleration in vertical direction (right)

Across all the data, the ATD seated in Seat 5 measured significantly larger loads in the head, chest, lumbar, and pelvis compared to the rest of the ATDs. This is a direct result of the seat being located over a rigid structure with no energy absorbing mechanisms present in either the seat or the subfloor. The other ATDs all experienced loadings of similar magnitudes and shapes and were significantly lower than Seat 5 because there were EA mechanisms present either in the seat or subfloor, or both. This demonstrates the effectiveness of the EA mechanisms to absorb energy and reduce loads transmitted to the ATD. While all the ATDs met the HIC and Nij criteria, only Seat 1 met the lumbar load criteria.

Model Development

A finite element model (FEM) of the L+C test article was generated to conduct pre-test predictions for the test and to also assess FEM capabilities for predicting the response of a composite airframe structure in a dynamic impact environment. The FEM of the L+C test article was developed and verified using a building block approach which incorporated coupon, component, and full-scale testing of the L+C test article. The full details of the L+C test article FEM development process can be found in [12] and [21]. Highlights from the FEM development process will be discussed in the current section to provide background on the model prior to discussion of the FEM's correlation to the second L+C test.

The FEM of the L+C test article was generated by creating models of each individual co-cured composite section of the test article. The geometry of these parts was matched to the computer aided design (CAD) used in part fabrication. The assembly of the test article and matching assembly process used in the FEM generation is shown in Figure 43. The section models were then bonded using a tied-contact within LS-DYNA. A failure limit was applied on the tied-contact to match bond-strength values determined from component level tests conducted on sections of the test article [12].

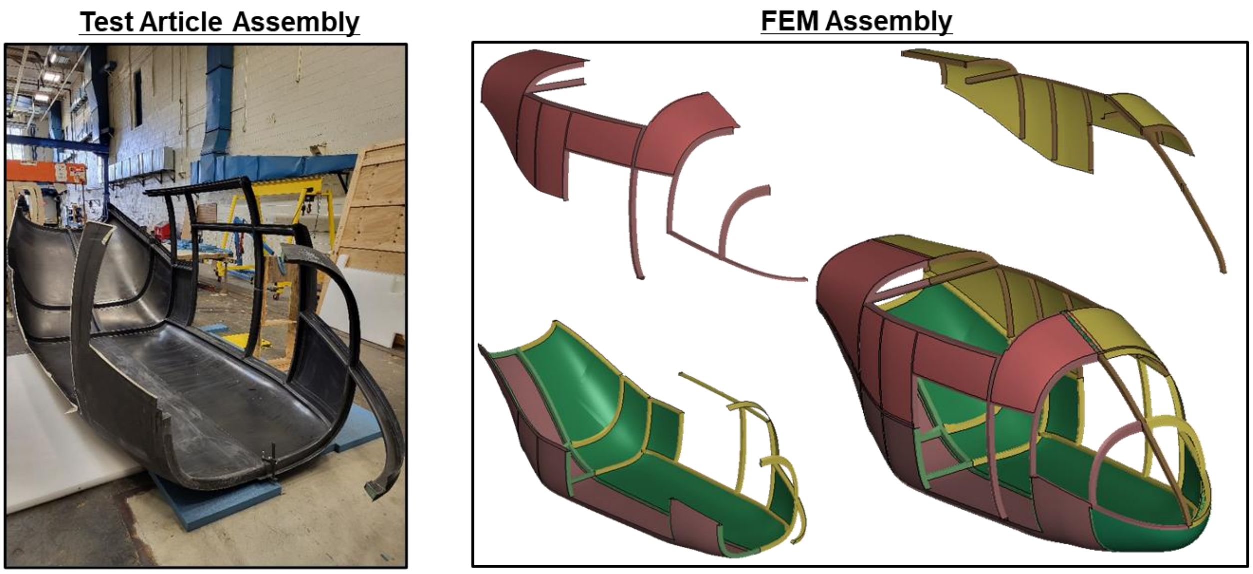

Figure 43. Assembly of the L+C test article and FEM.

Static coupon material testing was completed on specimens of the composite material used in the L+C test article in order to define the material properties within the FEM. Tests were conducted on the material at 0°, 45°, and 90° in both tension and compression. The composite material was represented in the FEM using the Mat-58 (laminated composite fabric) material model within LS-DYNA. Material stiffness parameters were defined based on the results of the coupon tests performed. The testing was then simulated using the generated material model to confirm the material response was accurately captured. Example results from test and simulation in 0° tension and compression are reprinted from [21] in Figure 44.

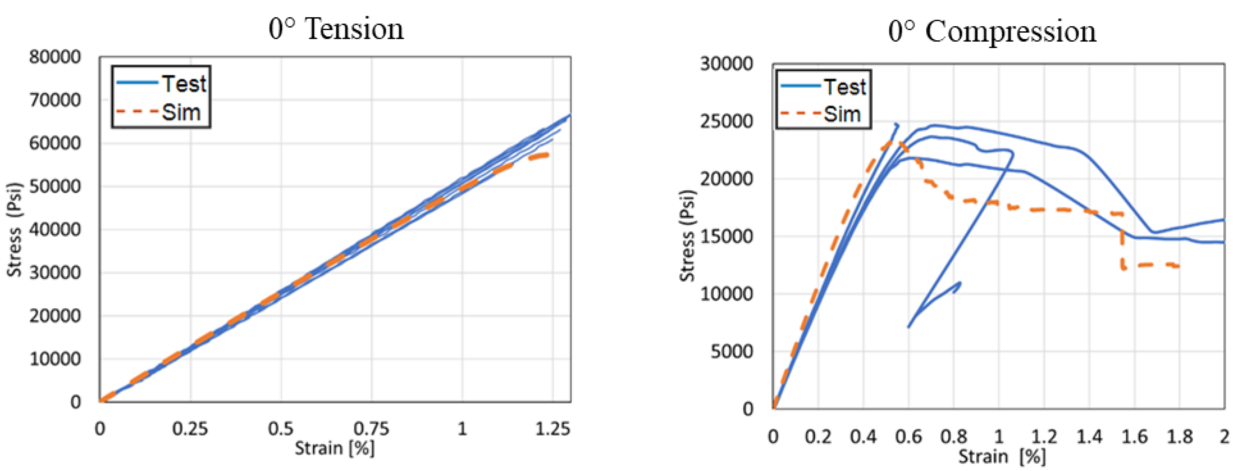

Figure 44. FEM correlation to static tension and compression coupon testing. Tension (left) and compression (right)

Dynamic component level testing was conducted on sections of a previously fabricated L+C test article structure. Testing was primarily conducted on frame sections, as these were the primary structural components of the test article. To characterize the dynamic failure response of the composite material dynamic three-point bend tests were conducted on these frame sections. These tests were conducted with a 115 lb. impactor and two different impact speeds, 10 ft/s and 15 ft/s. The 10 ft/s test was selected to induce damage into the frame without completely splitting it in half. The 15 ft/s test was selected to break the specimen in half during impact. High-speed 3D-DIC was used to measure surface strain during impact and to calculate a failure strain limit for use within the Mat-58 material model. An image of the 10 ft/s dynamic three-point bend test with principal strain overlaid is shown within the Photogrammetry section of this report in Figure 33.

The L+C structural material model was updated using the failure strain calculated from test data. The three-point bend tests were then simulated to evaluate the effectiveness of the model to predict brittle fracture in these dynamic loading conditions. Results comparing impactor acceleration between test and simulation in each three-point bend test condition is reprinted from [12] in Figure 45. With the updated element erosion limits defined, the FEM predictions closely matched measured test response of the composite beam section in both the partial damage (10 ft/s) and full-fracture (15 ft/s) condition.

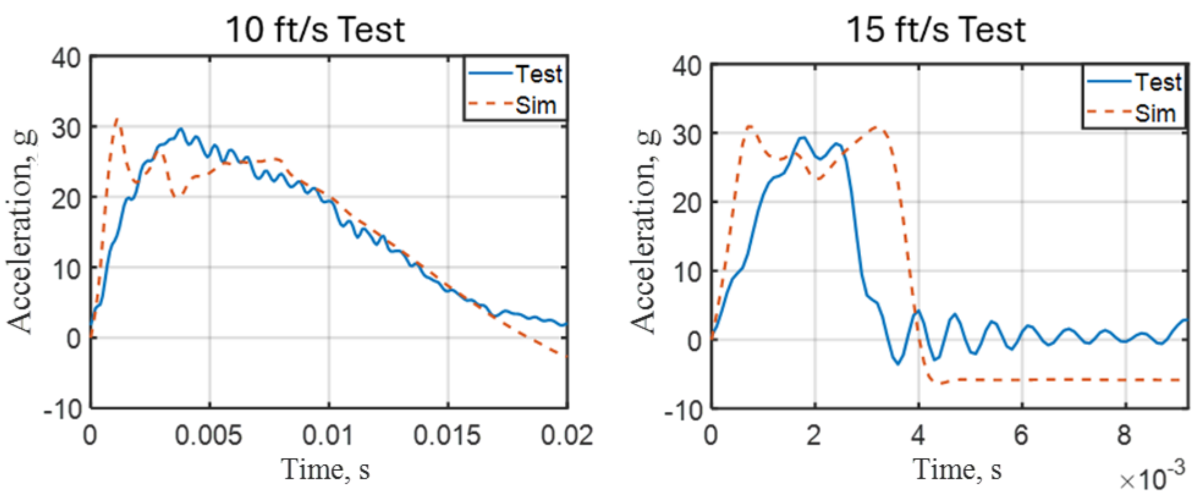

Figure 45. FEM correlation to impactor acceleration from dynamic three-point bend testing. 10 ft/s (left) and 15 ft/s (right)

The FEM of the L+C test article was then simulated in the conditions recorded from the L+C #1 test and the predicted structural response was compared to that of the physical test article. A comparison of structural deformation and damage between the test article and FEM is reprinted from [12] in Figure 46. With the composite structure material model calibrated using coupon and component level test data, the developed FEM of the L+C test article was able to closely predict the composite brittle fracture recorded throughout the airframe during the L+C #1 test. The vehicle FEM captured the fracture of the B-pillar and aft cabin section collapse. The collapse of the front starboard cabin section, due to the slight yaw at impact, was also predicted. These results showed the L+C test article FEM could predict structural failures; simulation of the L+C #2 test provided a means of determining whether the FEM could also effectively predict low levels of damage within the airframe

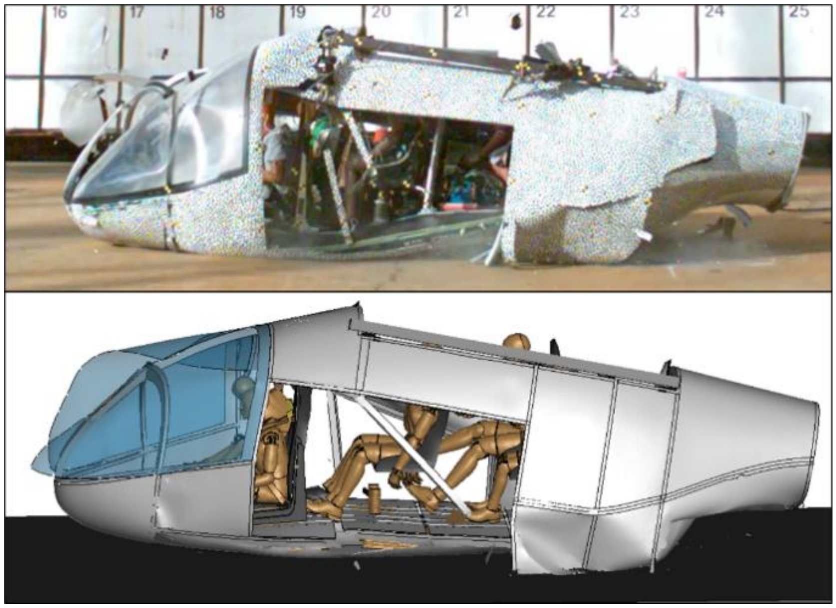

Figure 46. L+C #1 test structural deformation and damage comparison between test and simulation. Test (top) and simulation (bottom)

FEMs of the subfloor and seat components used within the L+C #2 test were developed in a similar manner to the building block approach taken with the L+C #1 test article structural FEM. Full details of the subfloor and seat FEM development can be found in [12] and [13]. Highlights from each are provided in this report in order to provide context for their use within the L+C #2 model.

A material model of the carbon-Kevlar composite material used in construction of the EA subfloors and crush tube components used in the NASA EA seat design was generated using coupon level testing of the material. Material parameters defined from these tests were implemented within a Mat-58 material model within LS-DYNA and the coupon tests were then simulated to confirm accurate prediction of the stress-strain response of the material. Example correlation results between test and simulation of the carbon-Kevlar coupon tests are reprinted from [13] in Figure 47.

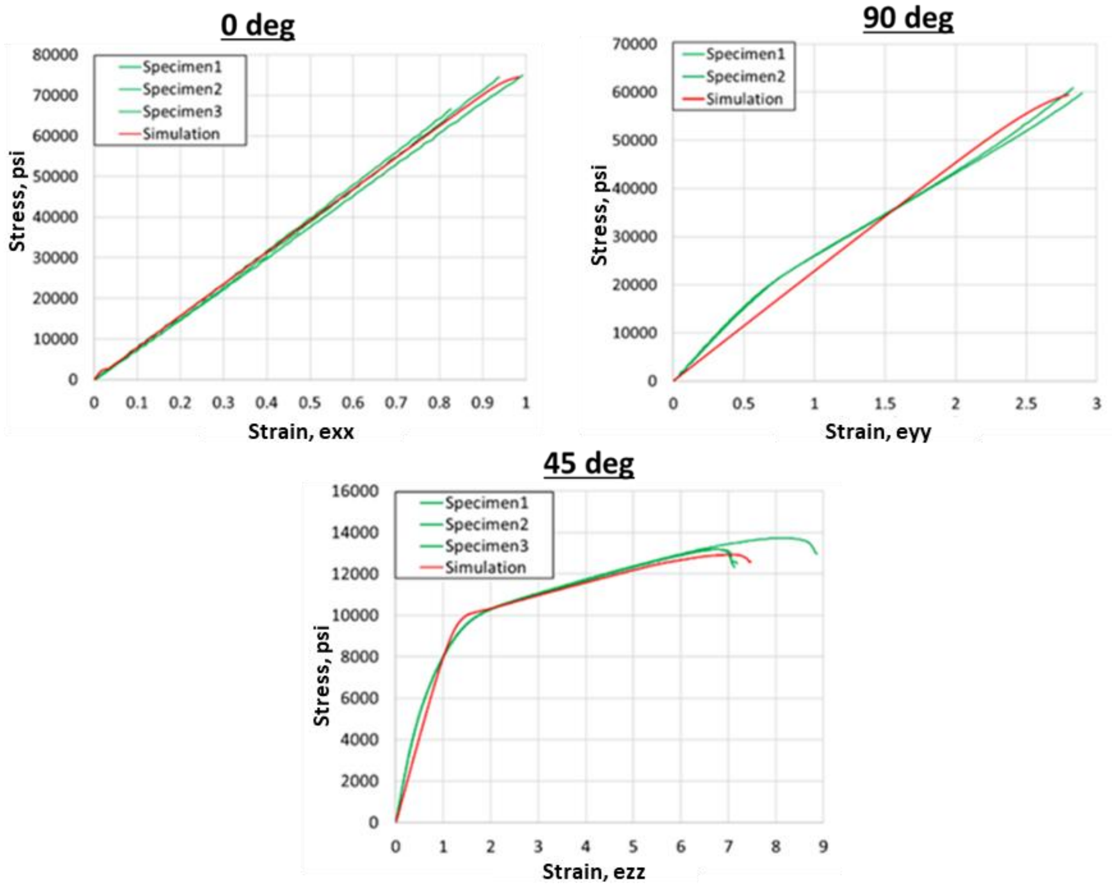

Figure 47. Stress-strain correlation results from carbon-Kevlar coupon level material characterization.

FEMs of the EA subfloor and seats were generated to accurately match the geometry of each component. CAD used in the component fabrication process was used to generate the FEM geometry of the NASA fabricated EA subfloor and seat EA components. Models of the COTS seat pans used in the testing were generated from 3D-scans taken of each seat. The generated FEM geometries of the EA subfloor and NASA EA seat are shown in Figure 48.

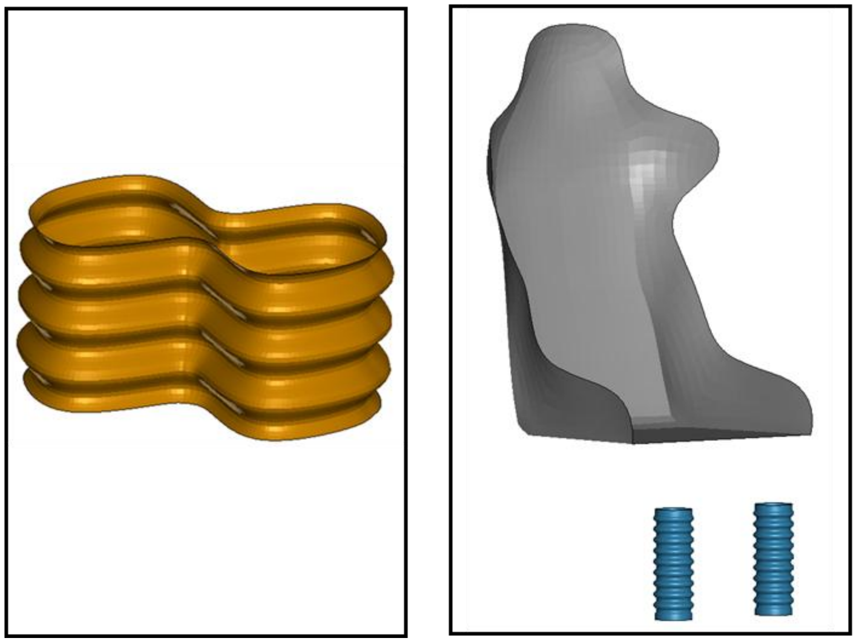

Figure 48. FEM geometries of the EA subfloor (left) and NASA EA seat (right) used in the L+C #2 test.

Dynamic impact tests were conducted on the EA subfloor and seat components to verify their predictive capability prior to implementation within the full test article model. Full details of this testing and analysis are provided in [13], [18], and [21]. The EA subfloor component was tested using a drop tower impact of a rigid mass onto the subfloor, the acceleration measured on the impactor was used as the primary means of correlation for this test. The seats were tested in a vertical drop tower impact environment with ATDs mounted on each seat. Lumbar load measured in the FAA H3 50^{th} ATD was used as the primary means of correlation for this testing. For the seat level model correlation, the LSTC Hybrid III 50^{th} version 151214_BETA was used to simulate the test conditions. The resulting correlation of each model is highlighted in Figure 49. The EA subfloor FEM was shown to closely predict the acceleration time history of the impacting mass, indicating effective prediction of the dynamic crush response of the component. The lumbar force of the H3 50^{th} ATD was also closely predicted in the NASA EA seat FEM.

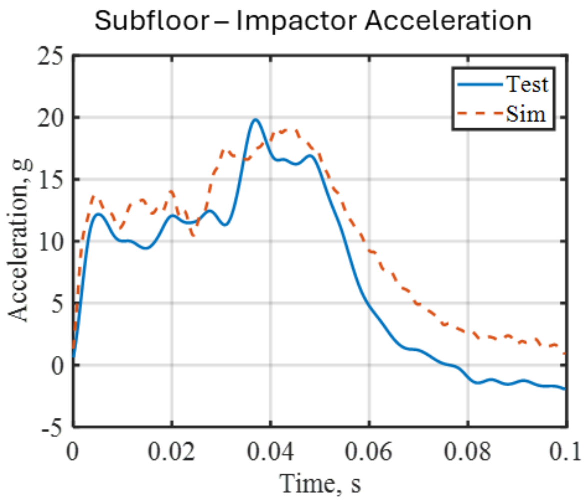

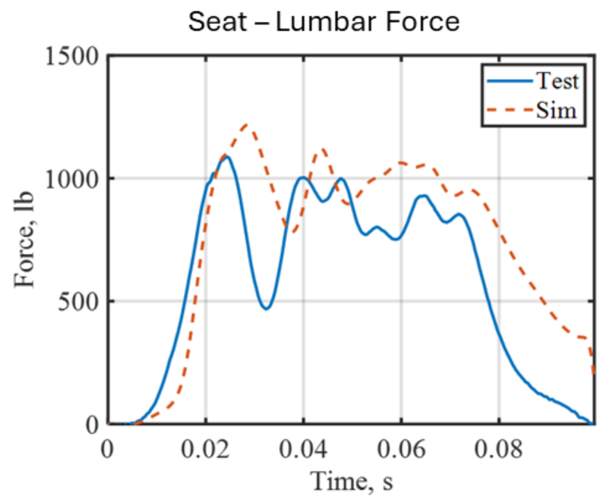

Figure 49. FEM correlation to component tests of subfloor (left) and NASA EA seat (right).

The EA subfloor and seat model's component models were integrated into the L+C test article FEM to match the configuration used in the L+C #2 test. The EA subfloor components were fixed to the vehicle skin and the floor components using tied contacts to represent the adhesive used in attaching these parts to the test article. The floor model, developed previously and verified to match the dynamic response of the floor used in the test article, is described in detail in [21]. Each EA subfloor model was arranged to match the location and orientation of the subfloors installed in the test. A FEM of the ESS fixture used in the rear subfloor of the test article was generated from 3D CAD used in part fabrication and an aluminum elastic-plastic model was used to represent the part material. This part was also attached using tied contacts between the airframe model and component. Aluminum beam elements were defined along the floor length representing the seat tracks used in the test. These elements were fixed to the floor using constrained nodal rigid bodies (CNRBs) representative of nut-bolt attachments used in the test article. The individual seat models were fixed to rigid sections defined on the seat tracks at the seat frame attachment locations, using constrained nodal sets between parts. The integrated cabin FEM is shown in Figure 50.

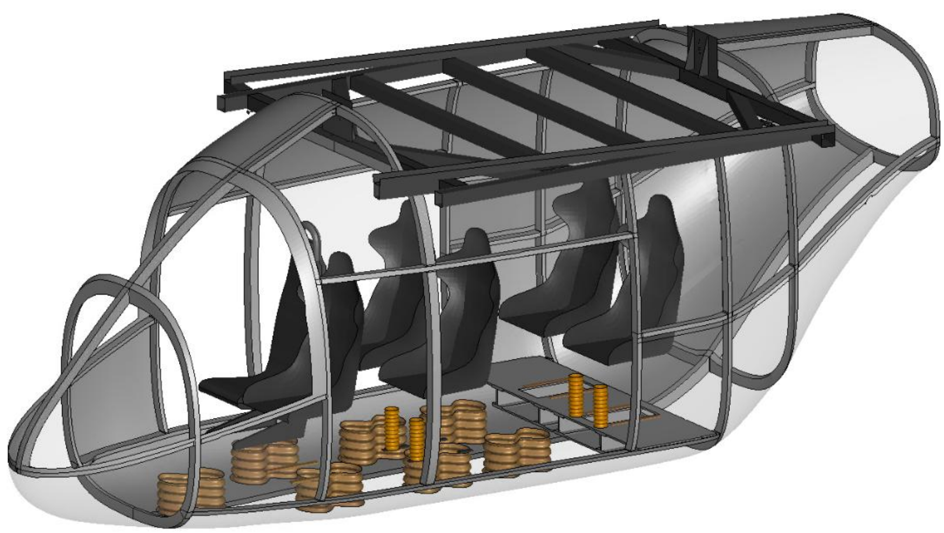

Figure 50. Integrated cabin FEM.

The ATDs included within the test were represented in the FEM using the publicly available ATD models distributed by Ansys. The LSTC Hybrid III 50th version 151214_BETA model [22] was used to represent both the H2 and FAA H3 ATDs in the test. The model was configured to match the upright posture of these straight-spined ATD's used in the test though some component differences between this model and the physical ATDs remain. For example, differences in neck part configurations between the model and Hybrid II ATD's would be expected to affect head/neck response. The primary focus of correlation between test and ATD simulations was lumbar force which was expected to be consistent between all three 50th ATD configurations evaluated. The H3 5th and 95h ATDs used in testing were represented by the LSTC Hybrid III -5th version 160920_V2 [23] and -95th version 151214.V3.03_BETA [23] models respectively. Each ATD model was positioned within the seats to match the approximate position of each ATD within the test article. This position matching was qualitative in nature. Belt models were fixed to each seat and fit to the ATD's matching the belt configurations used during the test. The seated ATD model setup used in the L+C #2 test article simulation is shown in Figure 51.

Figure 51. Seated ATD FEM setup.

The final additions made to the test article FEM to match L+C #2 configuration were the inclusion of the lifting hardware, windscreen, and point masses at the ballast locations. A FEM of the lifting hardware was generated from the CAD model used to fabricate the component. The lifting hardware was assigned as a rigid aluminum material model and was rigidly fixed to the airframe FEM. The windscreen FEM was similarly generated from the CAD used to fabricate the component and an elastic-plastic polycarbonate material model was used to define its properties. The windscreen was attached to the airframe using tied contacts representing the bonding agent used to attach the components. Added masses used within the test article at the tail and battery locations, along with mass for non-structural test components such as the DAS system were represented as nodal masses within the model rigidly fixed to the surrounding structure using a constrained nodal rigid body. The complete L+C #2 test article FEM is shown in Figure 52

Figure 52. Complete L+C #2 test article FEM

The L+C #2 test was simulated using the test-measured impact conditions of the vehicle which included horizontal velocity, vertical velocity, pitch, yaw, and roll. To conduct the simulation, the vehicle model was first oriented to match the measured impact angles. Next, the vehicle FEM was pre-loaded under gravity for 0.1 seconds in order to properly load the ATD occupants into the seats prior to impact, and the vehicle was held in place by rigid enforcement at the lifting hardware attachment points. After the preload phase was complete, velocity was applied to the complete test article FEM, matching the impact speeds measured in the test. To simulate the impact environment a representative concrete surface model was generated below the initial vehicle location. Simulation of the updated L+C test article model was performed using LS-DYNA MPP version 14.0 on a Linux Computer cluster. The simulation was carried out to a termination time of 0.4 seconds using 24 processors and had a run time of 115 hours.

Model Results

An image sequence of the structural response of the L+C airframe during the L+C #2 impact comparing test to simulation predictions is shown in Figure 53. The image sequence shows the airframe at the point of initial impact with the ground, at peak vertical deflection, and during the rebound. At each phase the simulation was found to closely predict the structural response of the airframe to the impact loads. At peak vertical deflection buckling can be observed in the floor section between the B- and C-pillars. This buckling is closely predicted by the FEM. Additionally the wrinkling of the composite skin behind the C-pillar is closely matched in simulation. After peak vertical deflection occurred, the L+C #2 test article exhibited a nose-up rebound off the impact surface. This response was predicted by simulation. As the vehicle rebounded off the ground, damage to the underbelly skin of the airframe could be observed with the underbelly damage being predicted by simulation. Overall, the FEM produced a high level of correlation to the test data and closely predicted material damage without overpredicting it. The close prediction of minimal material failure was an important observation, as it confirmed that the previous calibration of the L+C FEM to testing with significant composite brittle fracture did not predispose the material model to overpredict failure. One notable area of damage not predicted by the FEM was the damage observed at the portside of the windscreen, which occurred during the rebound of the vehicle. Through the examination of the test videos, this damage was confirmed to be caused by impact of the test swing cables with the windscreen. The swing cables were not explicitly simulated in simulation as they are considered external to the impact event intended to be analyzed and thus that interaction was not captured.

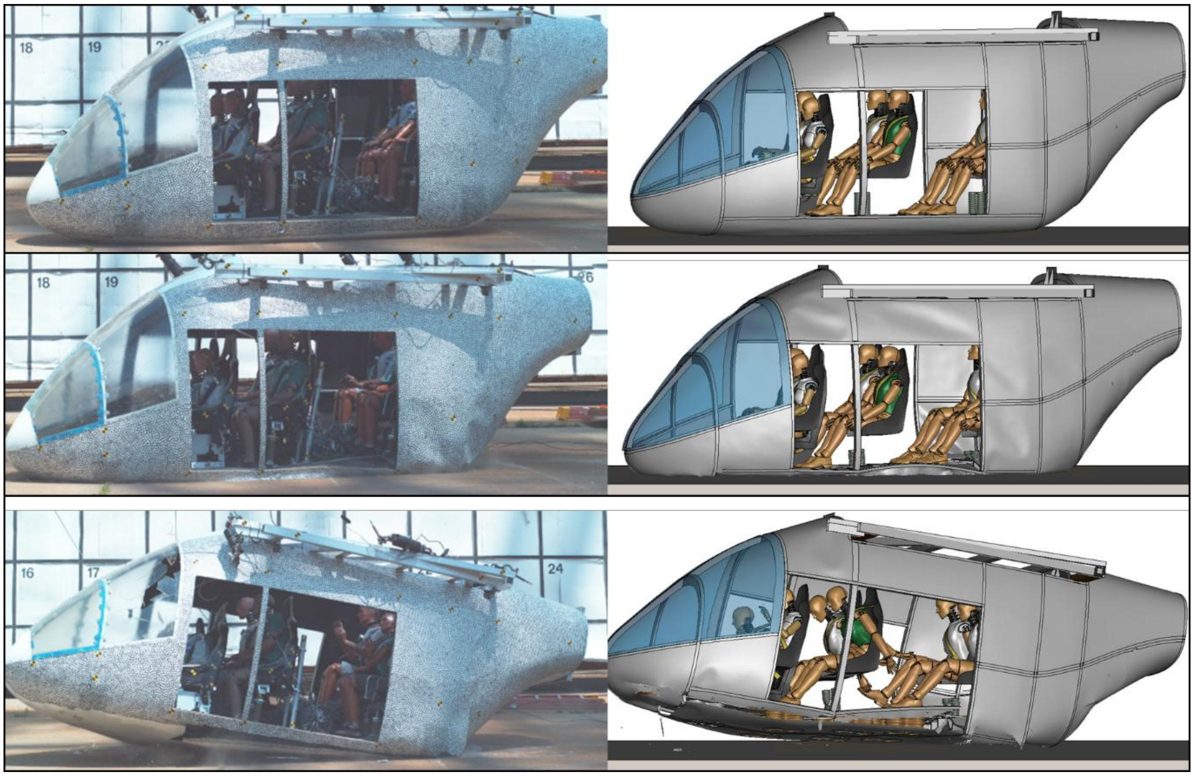

Figure 53. Test image sequence comparison to simulation prediction. Test images (left) and simulations (right)

A comparison of acceleration response measured on the test article overhead mass to that predicted by simulation is shown in Figure 54. The overhead mass can be effectively considered rigid relative to the rest of the test article and thus provides an effective point to look at overall kinematics of the test article during impact. Although horizontal acceleration was generally of low magnitude and highly oscillatory during the impact event, some general observations between test and simulation in this direction can be made. The time history of the simulated response generally matches the shape, with an initial rise up to 0.02 s followed by steady oscillations dropping off after approximately 0.06 s. Simulation slightly underpredicted the initial peak acceleration, but generally predicted the steady state acceleration oscillating around 10 g. In the lateral direction, the simulation again closely predicts the general shape of the acceleration time history, with a short initial peak at approximately 0.01 s, followed by a larger acceleration spike at 0.02 s with a steady drop off to 0.06 s. The peak lateral acceleration was slightly overpredicted by simulation. The vertical acceleration response was the direction most closely predicted by simulation. The phase, shape, and peak values were closely matched between test and simulation. The test showed an initial peak acceleration of 26 g at approximately 0.01 s, a second peak of 48 g at 0.02 s, and a fast drop in acceleration after that, all of which were closely predicted by simulation.

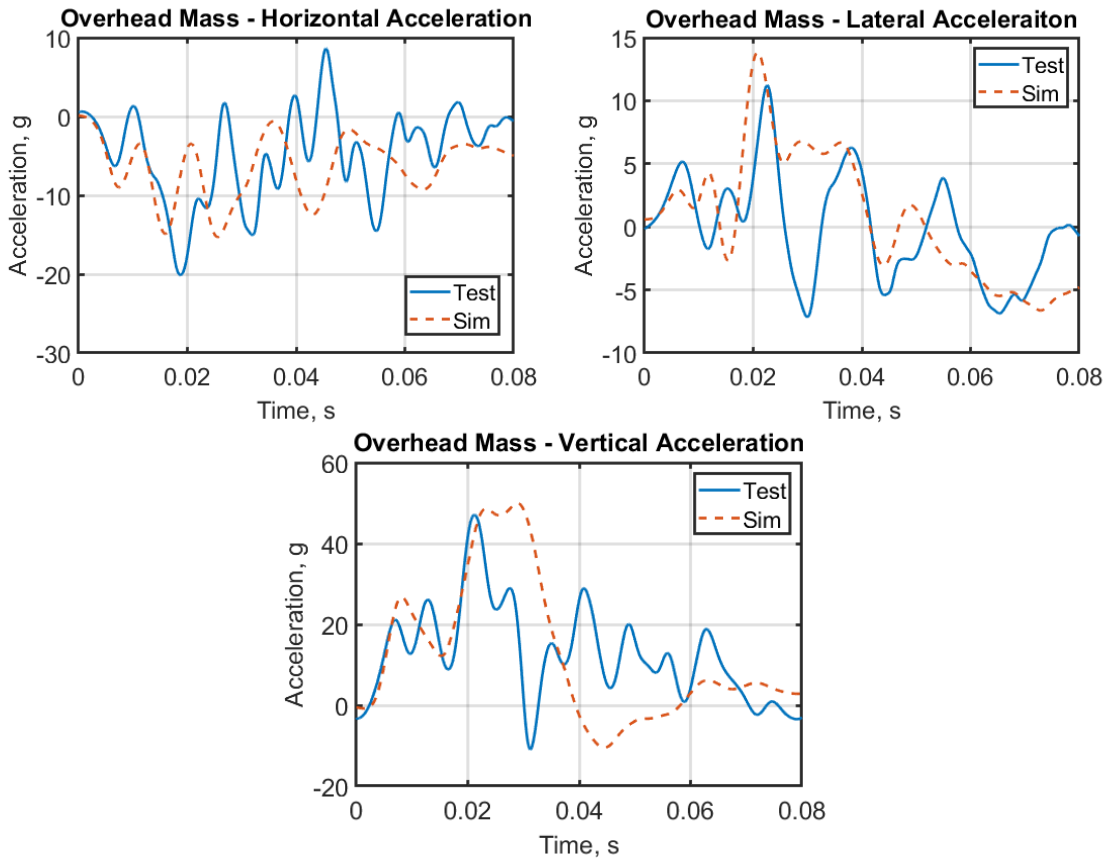

Figure 54. Overhead mass acceleration time history comparisons.

Examining areas in the extreme forward and aft portions of the airframe structure, the vertical acceleration in the front starboard A-pillar (forward-most location) and tail (aft-most location) are compared between test and simulation in Figure 55. Similar to the correlation observed in the overhead mass, the shape of the acceleration response is predicted in both airframe locations. In the front starboard A-pillar, two distinct acceleration peaks were recorded in test; this shape was closely matched by simulation though the absolute peaks were slightly underpredicted by the model. The acceleration in the tail exhibited more of a square shape, rising to approximately 10 g and holding for the first .08 s of impact. In addition to matching the acceleration shape, the peak and steady state acceleration values were predicted by simulation in the tail section.

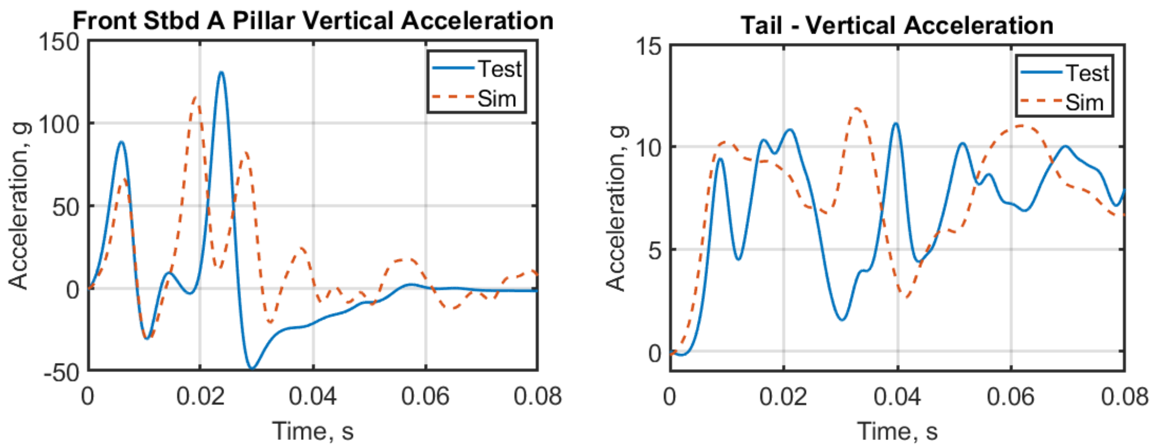

Figure 55. Airframe structural acceleration time history comparisons. A-pillar (left) and tail (right)

To interrogate the predictive capability of the combined airframe and integrated component FEMs, the vertical acceleration across the length of the vehicle floor is compared between test and simulation in Figure 56. In line with previously discussed acceleration correlations, the shape of the predicted acceleration was similar to test accelerations across each floor location, with the primary differences being in the magnitudes of the peak values. The front floor location was closely predicted, with the predicted peak acceleration of 60 g closely matching that measured in test. The location below Seat 4 showed the highest discrepancy between test and simulation, with the simulation underpredicting peak acceleration by 10 g. The seat at this location was the NASA EA seat which did not stroke during the test. This result was an artifact of the test setup and although the seat stroke was locked in simulation to approximate what occurred during the test, the exact binding mechanism has not been replicated. The discrepancy in floor acceleration is likely a result of slight stroking of the seat prior to it binding, as any partial stroking of the seat offloads the mass above the floor, thus increasing the acceleration applied through the subfloor. The high peak acceleration measured in the rear floor location over the simulated rigid ESS installation was effectively identified by simulation, indicating the capability of the FEM to identify effects of subfloor stiffness changes on acceleration loads transferred into the seat.

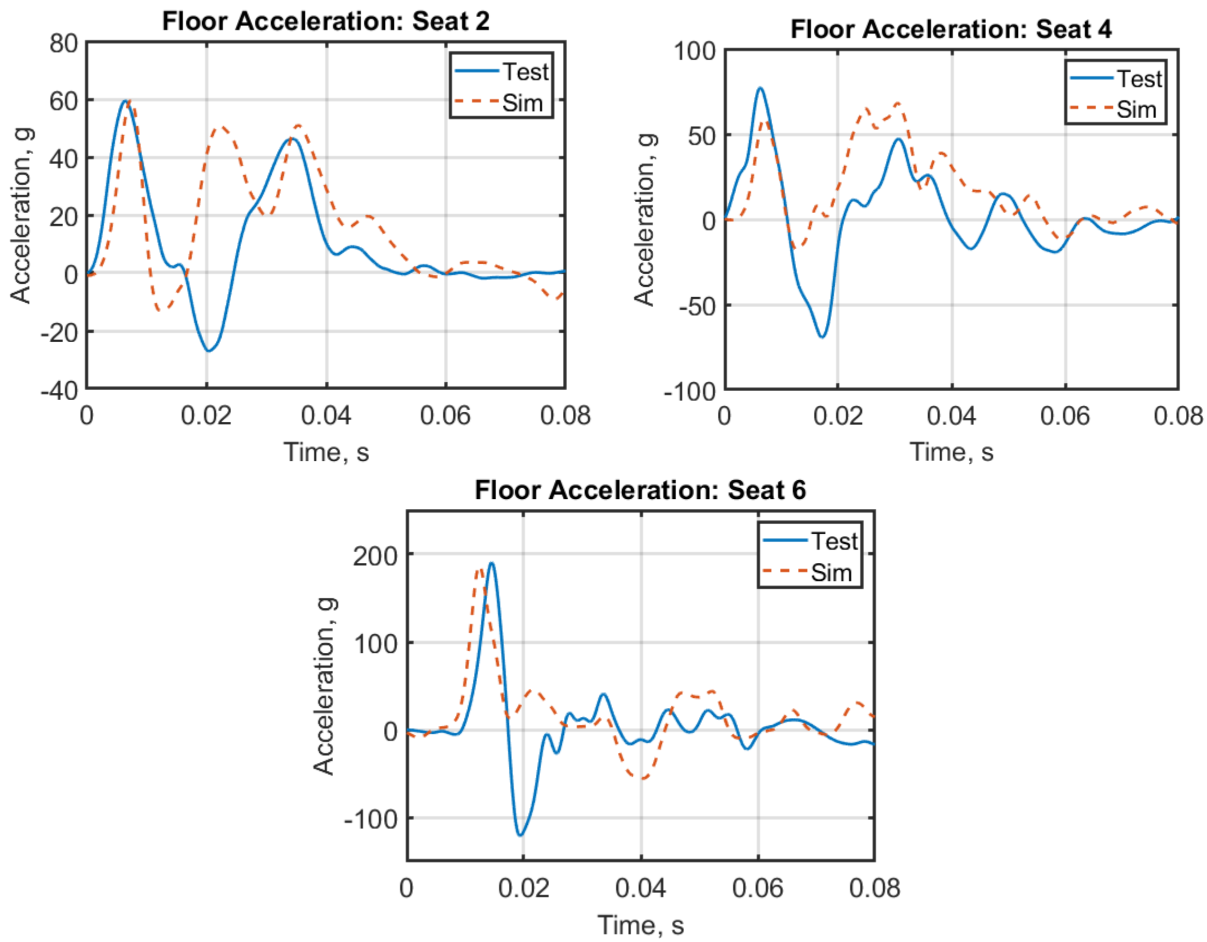

Figure 56. Floor structural acceleration time history comparisons.

A comparison between lumbar force measured in test and simulation at the Seat 2 location is shown in Figure 57. This location featured a composite seat bucket with rigid base and a H3 5th ATD as the occupant. The overall force time history shape was similar between test and simulation, though the simulation predicted a lower initial peak force and longer duration. The difference in initial peak lumbar force is likely due to a possible discrepancy in ATD spine position relative to the seat or a slight difference in seat stiffness, since differences in acceleration applied through the vehicle can be ruled out due to the floor accelerations closely matching at this seat location. Although the initial peak was underpredicted, the overall peak lumbar force was closely predicted by simulation later in the impact, resulting in similar prediction of overall occupant injury risk by test and simulation in this seat location.

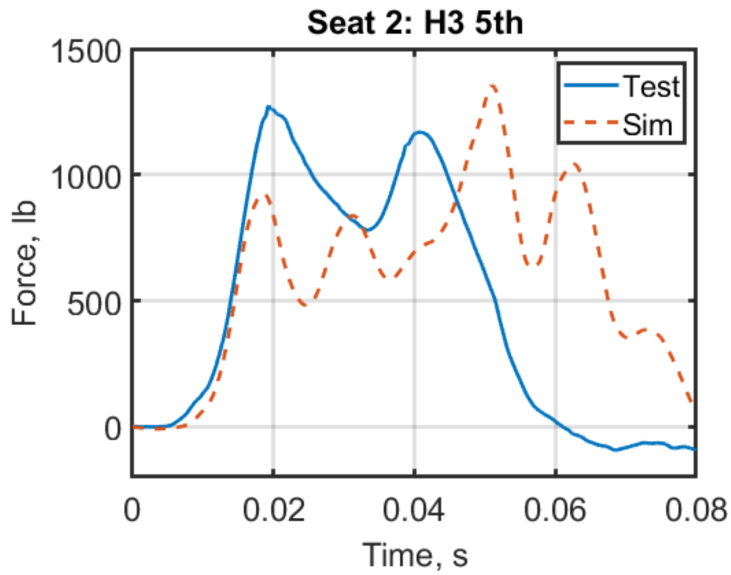

Figure 57. Lumbar force time history comparison for Seat 2 – H3 5th ATD.

A comparison between lumbar force measured in test and simulation at the Seat 3 location is shown in Figure 58. This location featured a composite seat with rigid base and a H3 50th ATD occupant. Unlike the previous seat comparison, the model generally overpredicted peak lumbar force though the shape and phasing of the predicted force was similar between test and simulation. The difference in predicted peak force can likely be attributed to differences in accelerations transferred into the seat through the vehicle FEM at this location. The adjacent Seat 4 was the NASA EA seat which did not stroke during the test. Issues with this stroking mechanism were not predicted by simulation and thus the amount of seat stroke and load on the crushable subfloors below differed between test and simulation. The floor section was shared between Seat 3 and Seat 4, so changes to one are likely to affect the amount of subfloor stroke in the other. The resulting differences in predicted lumbar load between test and simulation in Seat 3 demonstrate the sensitivity of these predictive tools to variability in the surrounding environment, such as the neighboring seat performance.

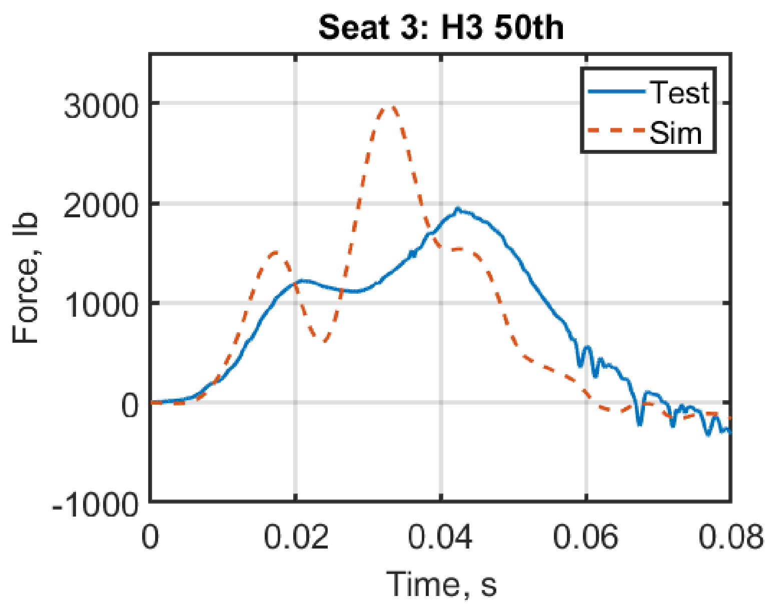

Figure 58. Lumbar force time history comparison for Seat 3 – H3 50th ATD.

A comparison between lumbar force measured in test and simulation at the Seat 5 location is shown in Figure 59. This location featured a composite seat bucket with rigid base overtop the rigid ESS subfloor with a H3 50th ATD occupant. The effect of the rigid subfloor under this seat location was clearly observed in both test and simulation, with both predicting high lumbar forces in this seat location. The simulation did predict a higher peak value as this may be an effect of the rigid part assumption used in the modelling of these seats. At these higher impact forces, the rigidity assumption in the seat base is challenged, so there is potential of deformation of the seat base which would absorb some impact energy and reduce peak force transferred into the ATD spine. The perfectly rigid seat frame assumptions used in the model do not account for this, and as such, may overpredict high lumbar loads.

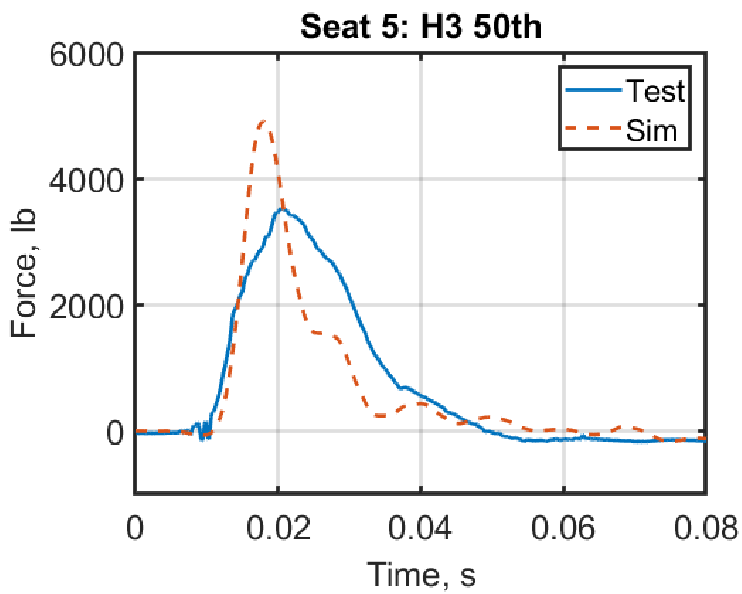

Figure 59. Lumbar force time history comparison for Seat 5 – H3 50th ATD.

A comparison between lumbar force measured in test and simulation at the Seat 6 location is shown in Figure 60. This location featured a composite seat bucket with NASA EA base overtop the rigid ESS subfloor with a seated H3 50th ATD occupant. Both test and simulation clearly predicted the reduction in lumbar force with the use of the NASA EA seat in this location. The simulation slightly underpredicted the initial peak lumbar force and crush initiation of the EA but closely predicted the overall peak lumbar force value. These results demonstrated the effectiveness of the model in predicting lumbar forces near the 1,500 lb. limit and its capability to identify changes in injury risk with the use of added EA systems.

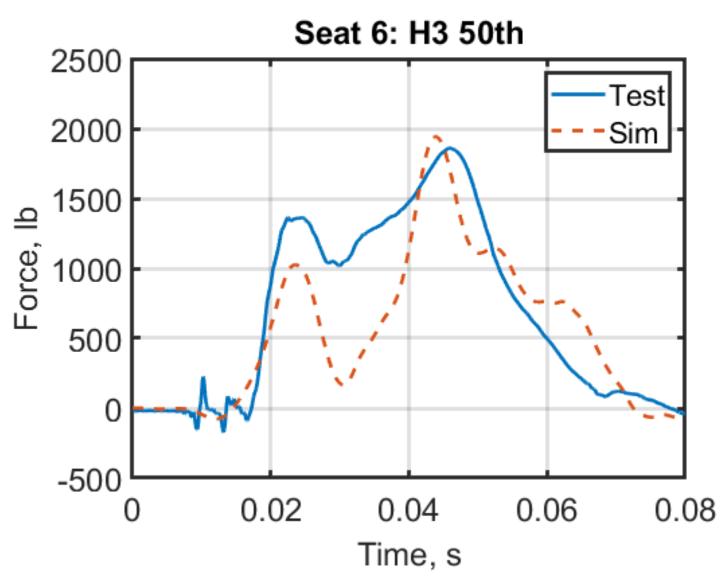

Figure 60. Lumbar force time history comparison for Seat 6 – H3 50th ATD.

Discussion

The results obtained from this test added to the suite of results obtained from the first full-scale test conducted in 2022. While there were many similar features between the tests, the differences were enough such that two distinct data sets were acquired. The acquired data is important since eVTOL vehicle crash data is not publicly available. For many researchers, other government entities, equipment OEMs, and other interested parties, having two sets of crash data, even if it is only of one government reference design, can help to provide answers and insight into factors affected during these types of events and allow progress to be made in a variety of industries affecting implementation of eVTOL vehicles in the U.S. airspace.

Noting the above statement, there were several variables that were intentionally changed to allow for an expanded and unique data set to be acquired from each of the two tests. The three major differences were the impact conditions, overhead mass configuration, and the underfloor experimental suite. The changes in these items between the two tests were intentionally made, and either due to results of the first test or identified as factors of interest as the research progressed toward the second test. The rationale for adding a yaw into L+C #2 was to investigate a three-dimensional impact condition. While, in real crashes, each crash condition is unique, and there are many factors that play a role in what those conditions are, the test aimed to simulate a more complex condition than simply vertical and horizontal velocities only. The added yaw, which was picked at 10 degrees based on the FAA Emergency conditions, specifically 14 CFR § 27.562 (b)(2) [11], was included to examine its effect on items such as airframe deformation, seat stroke and energy absorber performance. The results obtained from the test confirm, to some extent, that adding this complexity changes the way items respond, which is best demonstrated by examining the lack of seat stroke in Seat 4. The overhead mass, as captured in the lifting hardware of the test article, was adjusted from the first test to represent changing assumptions in the wing performance and ESS location. As the first test demonstrated risk of cabin collapse due to high overhead mass, the second test assumed the use of a frangible wing design which would offload the majority of wing and rotor mass during impact. In addition, the ESS mass was moved from the overhead to the underfloor location. Lastly the subfloor design was updated based on results of the L+C #1 test to work in better unison with the seat EA systems.

In parallel to full-scale vehicle impact testing, researchers in the group have been conducting component-level drop testing on ESS components [16-17] to determine response metrics of ESS subjected to various dynamic impact conditions, some of which were partially based on the L+C #1 data. In the developmental stages of determining the experimental suite to be included on the test, it was determined that collecting data on ESS (simulated) structures from a full-scale test would add relevance to the component level data that was being generated - all of which could be coordinated into additional follow-on test or modelling efforts. During the test article buildup, care was taken to replicate, to the best extent possible, an underfloor installed ESS configuration that may represent an actual installed condition. The resulting loading level data collected from this experiment, in conjunction with the performance of the component level ESS testing, paints a more complete picture of the performance of these components under crash-type loading, and is intended to provide at least some guidance to OEMs, installers, regulators and other interested parties.

As the full-scale test gave opportunity to test several experiments at the full-scale level, one notable result was unforeseen prior to test conduct. Specifically, the lack of stroking in the EA tubes from Seat 4 in the middle row was not anticipated during test planning and execution. The three-dimensional impact conditions, combined with the interactions between various components of the fuselage structure, subfloor structure and ATD, led to binding in the seat rails, which is the primary reason for this lack of stroke. It is important to note that while this was an unforeseen test event, it was only identified in the full-scale test. Vertical drop tower testing utilizing the same seat and subfloor configurations and a rigid floor structure showed stroking of the seat EA and crushing of the subfloors, suggesting that the designs, should they have performed nominally in the full-scale test, would have worked at a system level to further reduce occupant loading. However, because of the increased complexity of the full-scale test, this result did not occur. In broader terms, it was only because this system was tested at the full-scale level, with all of the associated complexities of the system response, that this result was produced. Thus, there is merit in utilizing full-scale testing to the maximum extent practical to obtain results pertaining to occupant protection for vehicles utilizing various EA systems.

The responses of the ATDs measured throughout the test article further demonstrate the importance in testing under complex and realistic loading environment to fully understand occupant response in the crash environment. One of the most interesting responses measured in this test was the lumbar load in the H3 95th in Seat 1. Although this was the heaviest ATD, it measured the lowest compressive lumbar force and was the only ATD that measured a peak lumbar force value below the relevant injury criteria limit. This is a response that would not have been identified by peak acceleration alone as this seat showed peak acceleration nearly matching that in Seat 2. Seat 2 had the lowest weight occupant and had a lumbar load which was almost 300 lb. higher than that measured in the heaviest occupant in Seat 1. The source of the low lumbar load in Seat 1 is hypothesized to be due to a combination of low seat height, seat stroking, and the addition of horizontal loading all resulting in a rotation of the ATD's pelvis as the legs were pushed upwards and torso forwards. This pelvis rotation would result in a higher lumbar moment, which was observed in this ATD along with an earlier onset of moment compared to the other ATD's in its vicinity. This effect was not observed in drop tower testing and is considered a response unique to combined axis loading of the occupant within this seat. Additionally, as mentioned previously, the performance of the combined subfloor and seat EA system was altered in the full-scale test environment. The ATD in Seat 4, which was positioned in a NASA EA seat, experienced a higher lumbar load than that measured in the neighboring Seat 3, due to binding of the seat stroke mechanism. Component level testing and analysis did not identify this risk and would have predicted a completely different story about occupant injury risk within each seat location.

The development of the test parameters associated with the second test, L+C #2, was heavily aided by development and execution of the L+C #1 test, which was conducted in 2022. As previously noted in various reports [10,12,21], the development of L+C #1 test relied heavily on component level testing and planning for test conditions and configuration relied heavily on computational simulations that were only partially validated at the time (e.g. the collapse of the roof was not predicted by the model). The test was the first attempt at examining the performance of both the subfloor design and seat EA tube at the full-scale level.

System level tests were conducted on leftover hardware from the airframe following the L+C #1 test in order to rectify these differences. From these tests, simulation updates were made, and subsequent post-test calibration simulations were run. These simulations showed improvements in the overall correlation, both in loading levels and in failure initiation and propagation. Though the first test was effectively represented after the simulation calibrations were completed, uncertainty remained as to whether the model predicted fracture because the physics of the material was properly grounded or that the simulations were calibrated to predict this specific test scenario.

The L+C #2 test provided a valuable data point with which to verify whether the vehicle FEM was robust in its ability to not only correlate to test results but be able to predict response across uniquely different conditions without the need for further test specific calibration. The L+C #1 test demonstrated the need to calibrate damage and failure parameters within composite material models through component level testing under relevant dynamic loading conditions, in order to effectively predict structural failures during the full-scale impact environment. The accurate prediction from the simulations of maintained cabin volume and minimal fracture in the L+C #2 test went a long way in answering this uncertainty, as it showed that the model, without any adjustment, was able to correctly identify conditions which did and did not produce fracture of the vehicle structure. This predictive capability is essential in potential use of these modelling capabilities to determine what impact conditions and vehicle configurations are potentially safe or harmful in the future

Additionally, when discussing predictive capability of the model in regard to the experiments onboard the L+C #2 test, an extensive understanding was gained at the full-scale level on the interaction between the seats, floors and ATDs in the test article. For example, when the crushable subfloor infinity design was redesigned post-L+C #1, there was great confidence in being able to predict the full-scale behavior from conducting only system level drop tests in the vertical direction only. Similar confidence was gained from the development of the new overhead mass/lifting system with regard to its effect on the overall vehicle structural response.

When comparing the L+C #2 test to simulation results, the developed vehicle FEM was found to accurately predict accelerative loads as they moved through the vehicle structure. Vertical acceleration was closely predicted across various locations measured on the vehicle, demonstrating an accurate representation of stiffness throughout the airframe model. Prediction of horizontal and lateral acceleration was not as accurate as that predicted in the vertical direction, though the overall magnitude of loading in these directions was much lower and more susceptible to slight discrepancies between test and simulation. For example, the friction value defined for the contact between the vehicle and impact surface is one of the primary drivers of horizontal and lateral acceleration of the vehicle FEM. This value was calibrated to the L+C #2 test results, but slight discrepancies in damage and total surface area of the vehicle belly in contact with the impact surface can affect the accuracy of this calibrated parameter. Thus, the generally representative prediction of acceleration shape, steady state magnitude, and duration exhibited by the model is reassuring that the physics of the vehicle structural response in the horizontal and lateral directions are reasonably well captured.

Within the vehicle cabin, the L+C #2 simulation demonstrated accurate prediction of vertical acceleration as it transferred through the airframe structure into internal components such as the subfloor. The model accurately predicted floor accelerations over differing subfloor designs, with close prediction of acceleration shape and peak value in floor sections over both the EA and rigid battery subfloors. This capability is essential in potential use of modelling to predict changes in occupant loading based on design features such as battery location and subfloor design. The one area the model was found to be limited was in prediction of floor acceleration near the NASA EA seat which did not fully stroke. The exact mechanism which led to the seat failing was not fully identified and therefore the precise response of the seat was not fully represented within simulation. The effect of this seat discrepancy on prediction of floor accelerations in the area of the seat, not just directly below it, provides an example of how sensitive these combined structural systems are to each component within them.

The ATD models simulated within the L+C #2 model did not precisely match the measured response in each occupant location, however they were able to effectively identify the changes to occupant injury risk with changes in occupant size, subfloor configuration, and seat type within the test article. Differences in lumbar force between the Hybrid III 5th and Hybrid III 50th within a rigid seat were accurately identified. In addition, the significant increase in spinal injury risk over the rigid battery box, and subsequent reduction in that risk with the use of the NASA EA seat were effectively identified. Limitations in the prediction of peak lumbar force were identified at high loads, well above the 1,500-lb. lumbar force criteria, where the model tended to overpredict force as it was increased. This overprediction was associated with assumptions made on the rigid seat frame model. Though this overprediction would not affect its ability to identify a pass-fail response of the 1,500-lb. criteria, should there be a need to accurately predict higher lumbar forces the rigid seat frame model assumption should be revisited.

This L+C vehicle design is not intended to be built, certified, or flown in the U.S. airspace. The test articles tested were designed and built to represent partial structural fuselage surrogates which may have differences to actual flying vehicle designs, which could include different materials, manufacturing methods and a host of others. However, the tests feature items common to a variety of designs (e.g. overhead mass, energy absorbing seats, subfloor space) and the data generated from these tests represent the impact levels that could encompass a large design space and thus should not be discounted. Moreover, the methodologies developed to test, simulate, calibrate, and validate the computational simulations are vehicle agnostic and methods provided can serve as a general guide to an OEM, aircraft certification officer (ACO), university student learning finite element analysis, or any other party intended to examine, analyze or interrogate computational techniques for the use in dynamic impact testing. Developing complex models that can accurately predict the majority of test events are difficult, and the methods presented demonstrate a way to achieve this objective for this program. Thus, this test serves as the culmination of an effort lasting over 5 years for eVTOL specific crashworthiness research at NASA Langley Research Center.

Summary

A team at NASA Langley successfully conducted an eVTOL full-scale crash test on the NASA reference Lift+Cruise vehicle design in June of 2025. This test was the second in a series of full-scale crash tests of the Lift+Cruise reference design, with the first of which occurred in 2022.

This Lift+Cruise test featured an almost identical vehicle body to L+C #1, however it contained different experiments, different impact conditions and different configuration assumptions. These differences were identified and refined following the first test through the use of advanced composite modelling efforts, a significant amount of sub-component testing, and lessons learned from the first test.

The test article featured various types of onboard occupants seated in a combination of rigid, energy absorbing and commercial seats. The test article successfully impacted the ground with three-dimensional component of impact velocity due to the inclusion of a yaw component. All data was successfully collected and is presented in this report. The data shows the EA systems functioned to limit the loads into the ATDs, however due to the large amounts of deformation or potentially the included yaw, the system-level experiment designed to allow for the use of both a crushable subfloor and a stroking seat did not occur as intended. However, the ESS experiment provided valuable data on subfloor level loadings, and the two seats that did stroke showed reduced loading into the occupants.

Simulations of the test showed the model was able to accurately predict loading levels, failure initiation and propagation and ATD response. These results show that with enough data and knowledge, simulations can predict test results relatively accurately.

The successful conduct of this test was the culmination of years of research efforts into eVTOL crashworthy systems by the researchers at NASA LaRC. The overarching research objectives were met through the development of two types of energy absorbing subfloors, the development of an energy absorbing seat tube, the development of advanced computational techniques for test prediction capabilities, and the inclusion of experiments meant to hold relevance in the eVTOL design space. It is hoped the data generated will be utilized to help to guide improved safety considerations for these (and other) types of vehicles, with the ultimate goal of revolutionizing air travel in the decades to come.

References

1. Fortune Business Insights. "Urban Air Mobility (UAM) Market Size, Share & Industry Analysis, By Vehicle Type (Air Taxi, Air Metro, Air Ambulance, Last-Mile Delivery, and Other), By Range (Intercity, and Intracity), By Operation (Piloted, Autonomous, and Hybrid), By End User (Ridesharing Companies, Scheduled Operators, E-Commerce Companies, Hospitals, and Medical Agencies and Private Operators), Regional Forecast, 2025-2032. https://www.fortunebusinessinsights.com/urban-air-mobility-uam-market-106344. September 8, 2025. Accessed September 24, 2025.

2. Shyr, M.C. et al. "Predictive Workload Model for Air Traffic Controllers during UAM Operations." 43rd AIAA/Digital Avionics Systems Conference (DASC). September 29-October 3, 2024. San Diego CA.

3. Pascioni, K. A. et al. "Propeller Source Noise Separation from Flight Test Measurements of the Joby Aviation Aircraft." Proceedings from the AIAA/CEAS Aeroacoustics Conference. June 4-7, 2-24. Rome, Italy.

4. Whiting, T. "NASA Prepares for Air Taxi Passenger Comfort Studies." https://www.nasa.gov/centers-and-facilities/armstrong/nasa-prepares-for-air-taxi-passenger-comfort-studies/. Accessed Sept 24, 2025.

5. National Transportation Safety Board. *Accident Investigation Final Report JOBY AERO INC JAS4-2*. NTSB Number: DCA22FA082. Released February 7, 2024.

6. Air Accidents Investigation Branch. *AAIB investigation to VA-1X, G-EVTL.* AAIB Number: AAIB-29460. Released August 9, 2023.

7. Silva, C., Johnson, W., Antcliff, K.R., and Patterson, M.D. "VTOL Urban Air mobility Concept Vehicles for Technology Development." Proceedings from the 2018 Aviation Technology, Integration, and Operations Conference, June 25-29, 2018, Atlanta GA.

8. Putnam, J.B., and Littell, J.D. "Evaluation of Impact Energy Attenuators and Composite Material Designs of a UAM VTOL Concept Vehicle." Proceedings from the Vertical Flight Society 75th Annual Forum and Technology Display. May 13-16, 2019. Philadelphia PA.

9. Littell, J.D., Putnam, J.B., and Cooper, M. "Simulation of Lift plus Cruise Vehicle Models to Define a Full-Scale Crash Test Campaign." Proceedings from the Vertical Flight Society 77th Annual Forum and Technology Display. May 10-14, 2021. Virtual.

10. Littell, J.D., Putnam, J.B., "A Summary of Test Results from a NASA Lift+Cruise eVTOL Crash Test," Proceedings from the Vertical Flight Society 79th Annual Forum and Technology Display, May 16-18, 2023. West Palm Beach, FL.

11. Federal Aviation Administration. "Emergency Landing Dynamic Conditions." 14 CFR § 27.562. Amended November 13, 1989.

12. Putnam, J.B. et al. "Component Characterization of an eVTOL Reference Model for Crashworthiness Studies." Proceedings from the Vertical Flight Society 80th Annual Forum and Technology Display, May 7-9, 2024. Montreal, Quebec, Canada.

13. Putnam, J. B. et al. "A Combined Test and Analysis Approach to Develop Energy Absorbing Systems for eVTOL Aircraft." NASA/TM-20260000121, 2026.

14. Kellas, S. et al. "Full Scale Crash Test of a MD-500 Helicopter with Deployable Energy Absorbers." Proceedings from the Vertical Flight Society 66th Annual Forum and Technology Display. May 11-13 2010. Phoenix AZ.

15. Abramowitz, a. et al. "Vertical Drop Test of a Shorts 3-30 Airplane." DOT/FAA/AR-99/87. November 1999.

16. Littell J.D. et al. "Dynamic Drop Testing of eVTOL Energy Storage Systems Part 1: Drop Test Data Summary." Proceedings from the Vertical Flight Society 81st Annual Forum and Technology Display. May 20-22, 2025. Virginia Beach, VA.

17. Littell, J.D. et al. "A Summary of Results from Phase 2 Dynamic Drop Testing of Energy Storage Systems for electric Vertical Take-off and Landing (eVTOL) Vehicles." NASA TM-20250006515. July 2025.

18. Littell, J., Putnam, J.B., Gardner, N.W., Hardy, R.C., "A Summary of Results from Vertical Drop Testing of Hybrid III and WIAMan ATDs." NASA/TM-2015-20250000911. November 1, 2025.

19. Society of Automotive Engineers (SAE), "Surface Vehicle Recommended Practice: Instrumentation for Impact Test-Part 1-Electronic Instrumentation," SAE J211-1, 2017

20. Bolukbasi, A. et al. "Full Spectrum Crashworthiness Criteria for Rotorcraft." RDECOM TR 12-D-12. Dec. 2011.

21. Putnam, J.B., Littell, J.D., "Simulation and Analysis of NASA Lift Plus Cruise eVTOL Crash Test," Proceedings from the Vertical Flight Society 79th Annual Forum and Technology Display, May 16-18, 2023.

22. Guha, S., "LSTC Detailed Hybrid III 50th Dummy Positioning and Post-Processing," Livermore Software Technology Corporation, MI, 2014.

23. Guha, S., "LSTC Detailed Hybrid III 5th Dummy Positioning and Post-Processing," Livermore Software Technology Corporation, MI, 2016.